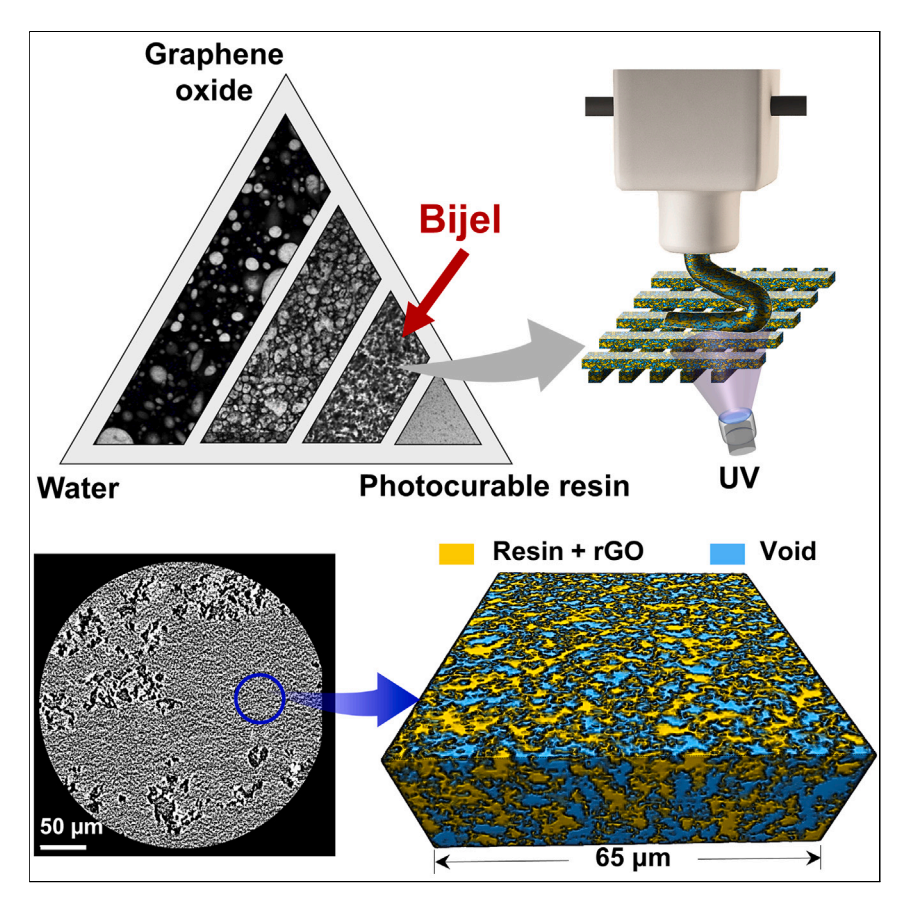
**Matter** 



# **Article**

# Morphology map-guided identification of bijel ink for producing conductive porous structures



Integrating conductive fillers into polymer matrices is critical for producing highly flexible and lightweight conductive materials for applications in sensing, tissue engineering, and energy storage/conversion. This work provides a straightforward template for producing the desired easy-to-process, printable, wearable conductive materials by identification of the inkability of bijels. Performance-related properties can be tuned through changing the porosity and filler loading.

Yifei Wang, Ciera Cipriani, Chia-Min Hsieh, ..., Miladin Radovic, Peiran Wei, Emily B. Pentzer

peiran@tamu.edu (P.W.) emilypentzer@tamu.edu (E.B.P.)

# Highlights

Morphology map was designed to illustrate different emulsion morphology

Printability of bijel was demonstrated by an inkability map

Wearable conductive materials with rapid RF heating response are readily achieved

The methodology has adaptability to different particle and fluid systems



Wang et al., Matter 6, 4066–4085 November 1, 2023 © 2023 Elsevier Inc. https://doi.org/10.1016/j.matt.2023.10.001







# **Article**

# Morphology map-guided identification of bijel ink for producing conductive porous structures

Yifei Wang,<sup>1</sup> Ciera Cipriani,<sup>1</sup> Chia-Min Hsieh,<sup>2</sup> Huaixuan Cao,<sup>3</sup> Anubhav Sarmah,<sup>3</sup> Kai-Wei Liu,<sup>4</sup> Zeyi Tan,<sup>1</sup> Micah J. Green,<sup>3</sup> Miladin Radovic,<sup>1</sup> Peiran Wei,<sup>5,6,\*</sup> and Emily B. Pentzer<sup>1,2,\*</sup>

## **SUMMARY**

Manufacturing of composites consisting of polymers and electrically conductive fillers is critical for producing wearable conductive materials. Here, we demonstrate the direct ink writing of bijels composed of bicontinuous water and resin phases stabilized by graphene oxide (GO) to fabricate wearable electrically conductive foams with excellent tensile performance. A morphology map was established to illustrate emulsion morphology and ink printability. After printing, conductive foams were readily obtained by resin curing, GO reduction, and water removal. The bijel ink can be printed and processed on different fabrics with excellent adhesion, and the obtained structures present an exceptionally rapid heating response to radio frequency; with only 4.0 wt % loading of nanosheets, temperature increased by 215.4°C in 1.0 s, outperforming previously reported particle/polymer composites. This work provides a roadmap for developing phase behaviors for fluid-fluid systems stabilized by nanoparticles, including printable bijels, and enables the 3D printing of wearable, porous, conductive materials without complicated pre/post-processing.

#### **INTRODUCTION**

Wearable conductive polymer composites have attracted increased attention because of their promising applications in sensing, 1,2 energy transport/storage, 3 biomedicine, <sup>4</sup> and so on. <sup>5,6</sup> These composites are generally composed of an elastic polymer matrix and conductive filler. The elastic matrix imparts high flexibility, which enables the material to recover its original shape after deformation, in contrast to the lack of recovery observed in conductive pure inorganic materials (e.g., metals, carbon nanotubes).<sup>8</sup> To further make materials wearable, researchers have recently focused on lowering the density of the structures to make them ultralight. This is accomplished using alternatives to metal-based fillers and/or introducing porosity into polymeric composite structures. 9,10 In such systems, carbon-based fillers are of particular interest for their excellent electrical properties, <sup>11,12</sup> chemical stability, <sup>13</sup> and noncorrosive nature, 14 which make them suitable for a variety of application spaces. Current methods to fabricate conductive composites/foams generally involve freeze-drying, <sup>15</sup> acid etching, <sup>16</sup> templated foaming, <sup>10</sup> or other harsh procedures. For example, Ge et al. 15 designed a porous sponge of reduced-graphene oxide/polyaniline for flexible pressure sensing and used this to detect human motion (e.g., squatting and rising); this system required freeze-drying to maintain the morphology of the prepared composite. As another example, Chen et al. 10 produced a composite structure of MWCNT (multi-walled carbon nanotube)/PS (polystyrene)/PMMA (poly[methyl methacrylate]) from a two-step melt blending process

# **PROGRESS AND POTENTIAL**

Traditional methods for producing conductive porous polymer composites often rely on sacrificial filler removal or templated foaming together with complicated, time-consuming, or environmentally unfriendly pre/ post-processing. This research introduces a pioneering approach to create printable, interconnected biphasic inks, streamlining the production of robust, highly porous foams without the need of sacrificial fillers, foaming agents, and harsh processing procedures. This study not only provides a new roadmap in leveraging fluid-fluid phase behaviors and 2D particle stabilizers for next-generation flexible conductors but also offers an efficient and scalable technique for producing wearable structures with tunable porosity, superior tensile performance, and electrical conductivity at low conductive filler loading.





at 200°C, followed by CO<sub>2</sub> foaming; the obtained porous structure could be applied to shielding of electromagnetic (EM) waves. The techniques used to produce these structures are optimized for individual materials and can be complicated/time consuming, energy intensive, poorly scaled, and dangerous and not suitable for rapid prototyping. Additive manufacturing and 3D printing are efficient techniques to produce targeted geometric designs and have been widely used for fabricating complex structures, including porous objects and those that are conductive. 17-20 Among the 3D printing techniques, direct ink writing (DIW) has garnered increasing attention because it can be performed at ambient temperature, and feedstocks (inks) with tunable composition can be readily produced. 17,21,22 Inks for DIW must possess appropriate rheological behavior to be successfully extruded from the printing nozzle and maintain the shape after printing (e.g., shear thinning and thixotropic); <sup>23–25</sup> further, the printed objects are commonly cured through solvent evaporation or chemical cross-linking to produce solid structures. <sup>22,26</sup> Porous objects can be prepared by DIW, most commonly when sacrificial components (e.g., particles or droplets) are used as fillers in the ink. 16,21,27 For example, our group previously formulated inks with carbon black, nanoclay, and thermoplastic polyurethane (TPU), which were printable by DIW; a porous, elastic conductive composite was prepared by removal of the clay with hydrofluoric acid and freeze drying. 16 Alternatively, emulsion-based inks can give porous objects upon removal of the solvents under relatively mild conditions, such as evaporation.<sup>28–31</sup> While promising, emulsion-based inks for DIW have, to date, produced mainly closed-cell foams, and composition of the structures produced is dictated by rheological behavior of the ink (e.g., filler and matrix compatibility, filler size, and vol % loading percentage), and thus concentrated emulsions and high internal phase emulsions (HIPEs) are most commonly used. For example, Sommer et al.<sup>28</sup> used concentrated decanein-water emulsions stabilized by chitosan-modified silica particles as inks for DIW; after printing, solvent was evaporated, and the printed skeleton was cured by cross-linking of chitosan in glutaraldehyde solution vapor for 2 days. In addition to closed-cell foams, such approaches to printing open-pore foams from emulsions<sup>32–34</sup> can be accessed. For instance, Minas et al.<sup>33</sup> prepared open-pore foams through octane-in-water emulsions stabilized by modified alumina and poly(vinyl alcohol), where the emulsion can be printed and dried at ambient temperature to achieve the porous structures. However, in these cases, thin polymer films may still exist between neighboring pores, 35 which may restrict interconnection-related performance (e.g., transport).<sup>36</sup> DIW additive manufacturing offers the possibility of tuning materials properties with the synergy of the macroscale geometry afforded by printing and the microscale porosity afforded by ink formulation while also integrating the functional properties of ink components (e.g., conductivity, catalytic activity, etc.). To realize such progress and, for example, produce low-density conductive structures relevant for various applications, significant advances in ink formulation and production are required.

In the present work, we provide a method to develop biphasic inks for DIW by constructing a morphology map composed of two fluids (water and photocurable resin) and 2D particle stabilizers (graphene oxide nanosheets). The morphology of the biphasic system (e.g., emulsion, concentrated emulsion, or bicontinuous emulsion) is established by optical and confocal fluorescence microscopy. By systematically evaluating the phase behaviors based on composition, we establish printability of inks and morphology and performance-related properties of printed structures. Successful inks can be extruded from a nozzle and maintain their shape, with appropriate rheological properties confirmed by rheometry. After printing, the resin phase is cured (i.e., cross-linked) using UV light to impart excellent elasticity; then the

https://doi.org/10.1016/j.matt.2023.10.001

<sup>&</sup>lt;sup>1</sup>Department of Materials Science and Engineering, Texas A&M University, College Station, TX 77840, USA

<sup>&</sup>lt;sup>2</sup>Department of Chemistry, Texas A&M University, College Station, TX 77843, USA

<sup>&</sup>lt;sup>3</sup>Artie McFerrin Department of Chemical Engineering, Texas A&M University, College Station, TX 77843, USA

<sup>&</sup>lt;sup>4</sup>Texas A&M Transportation Institute, 1111 Rellis Pkwy., Bryan, TX 77807, USA

<sup>&</sup>lt;sup>5</sup>Soft Matter Facility, Texas A&M University, 1313 Research Pkwy., College Station, TX 77845, USA

<sup>&</sup>lt;sup>6</sup>Lead contact

<sup>\*</sup>Correspondence: peiran@tamu.edu (P.W.), emilypentzer@tamu.edu (E.B.P.)





Figure 1. Scheme illustrating the design of the morphology map of inks composed of graphene oxide (GO), water, and photocurable resin

The map demonstrates different fluid-fluid phase behaviors and dictates the optimized composition of the bijel ink for direct ink writing (DIW) printing. 3D printing of the bijel ink can produce wearable conductive porous structures with excellent RF heating response.

nanosheets are chemically reduced, and water is removed by evaporation. We demonstrate that electrical conductivity and tensile performance are dependent on composition. Bicontinuous emulsion (i.e., bijel) inks are produced when the resin/water mass ratio is at 1.4-1.5 with 4.0-6.7 wt % nanosheets or at 2.2-2.3 with 2.5-4.3 wt % nanosheets. These inks can be used to fabricate high-surfacearea, low-density, conductive, highly interconnected porous structures that can be freestanding or printed onto different clothing materials with good adhesion. These structures exhibit an exceptionally rapid heating response to radio frequency at reduced particle loading and input power, outperforming similar compositions prepared through traditional methods. <sup>37–39</sup> These results highlight the critical importance of the bijel structure, which guarantees highly interconnected void domains and excellent conductive filler percolation that traditional emulsions cannot give. Importantly, we demonstrate that other nanosheet surfactants, specifically transition metal carbides (Ti<sub>3</sub>C<sub>2</sub>T<sub>z</sub> MXenes), can be used in partial replacement of the graphene oxide (GO) nanosheets to access the same morphology map and produce composite structures. This work provides a new roadmap in structure-processingproperty relationships of 3D-printed porous polymer composites (Figure 1), which not only provides a facile and scalable method for fabricating ultralight wearable conductive structures with excellent properties but also opens a new horizon of wearable conductive materials with tunable porosity, excellent tensile properties, and electrical conductivity at low nanofiller loading.

# **RESULTS AND DISCUSSION**

We use GO nanosheets as 2D particle stabilizers to establish fluid-fluid phase behaviors of viscous systems, specifically water/photocurable resin mixtures. GO nanosheets are comprised of a 2D honeycomb carbon skeleton with carbon-carbon double bonds and oxygen-containing functional groups, with properties such as conductivity dictated by the extent of oxidation. House, the nanosheets have an affinity to non-polar and polar phases, such as the oil-water interface, and they can be employed as particle stabilizers for Pickering emulsions. Indeed, the interfacial activity of GO is well established, and our previous work demonstrated that GO stabilizes emulsions of fluids with low viscosity (e.g., toluene in water) and emulsions prepared from relatively high-viscosity liquids (e.g., ionic liquid-containing emulsions). On note, concentrated aqueous dispersions of GO are non-Newtonian and can help with modifying the rheological behavior of a Newtonian fluid (e.g., resin) to impart non-Newtonian behavior: the



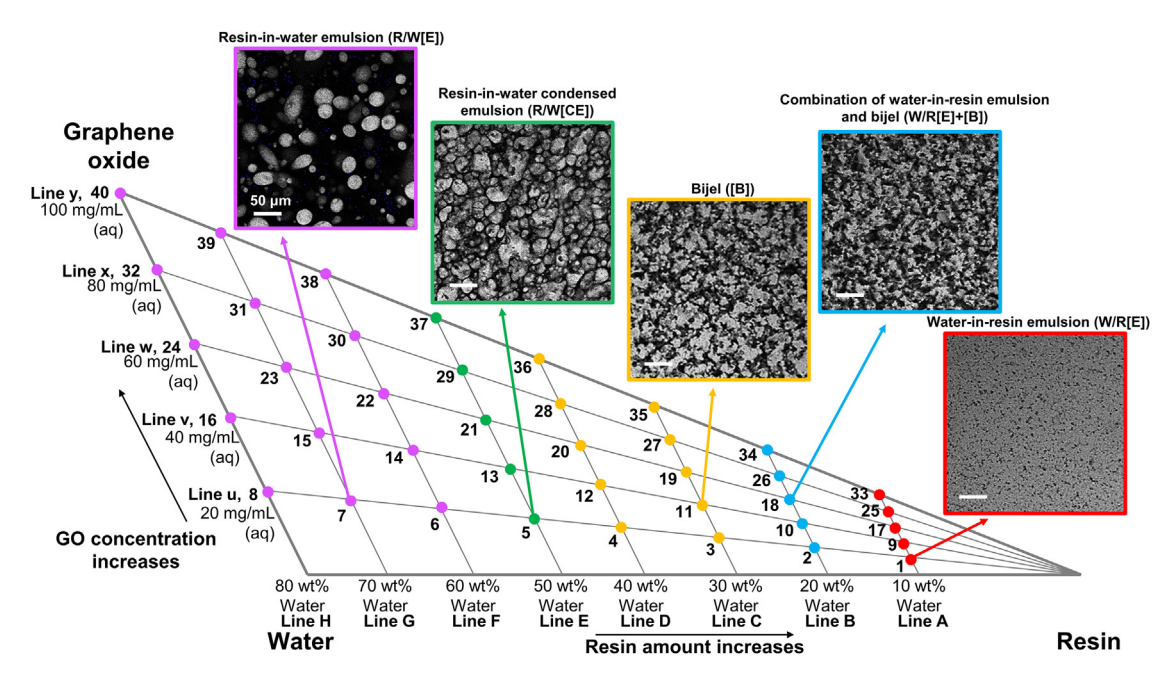


Figure 2. Morphology map composed of GO, water, and resin

Phase behavior is identified with different colors: water-in-resin emulsion (W/R[E], red), combination of water-in-resin emulsion and bijel (W/R[E]+[B], blue), bijel ([B], yellow), resin-in-water condensed emulsion (R/W[CE], green), and resin-in-water emulsion (R/W[E], magenta). Scale bars, 50 µm. Points along longitudinal lines have the same water content (wt %, lines A–H), and points along lateral lines have the same GO/water concentration (lines u–y).

low-dimensional particles enable elastic deformation of the solution mixture in response to external applied stress (e.g., particle-particle interactions).<sup>47</sup> In the system described below, GO nanosheets serve multiple purposes: particle surfactant, rheological modifier, and precursor to electrically conductive nanosheets (e.g., upon chemical reduction).

#### Morphology map construction

A morphology map composed of different mass ratios of water/resin/GO was constructed to identify the impact of composition on the printability, morphology, and conductivity of the resulting structures (Figure 2). A low-cost commercially available resin (Formlabs Elastic 50A resin) with photo-curability suitable for DIW layer-by-layer UV curing was selected. For experimental convenience, GO/water dispersions with concentrations ranging from 20-100 mg/mL at 20-mg/mL intervals were prepared (higher concentrations are inaccessible because GO precipitates). The system mass was held constant at 1,000 mg, and water mass ranged from 100-800 mg at 100-mg intervals. The nanosheet mass and resin mass were selected accordingly, and 40 sample compositions were used, as shown in Table S1. These compositions reside within the area of an obtuse triangle on a full morphology map (Figure S1), which is used to describe the system in the following discussion. All samples were prepared by first preparing aqueous dispersions of GO nanosheets and then adding the appropriate amount of resin and agitating the mixture using a planetary mixer (2,000 rpm for 1 min). Optical microscopy and confocal fluorescence microscopy were used to identify the microstructures of different compositions (samples) in this morphology map. The images obtained by optical microscopy shown in Figure S2 illustrate the microstructures. Confocal fluorescence microscopy imaging gives better-quality images (e.g., more easily distinguishable; Figure S3) because the resin itself is fluorescent.





A morphology map can be constructed, with different microstructure areas identified using optical and confocal microscopies. As shown in Figure 2, for samples from line A to line H, increasing the ratio of water/resin leads to the fluid-fluid microstructure changing from a water-in-resin emulsion (W/R[E]) to a resin-in-water emulsion (R/W[E]), with bijel and emulsion combination (W/R[E]+[B]), pure bijel ([B]), and condensed resin-in-water emulsion (R/W[CE]) behaviors transitioning between the highest ratios. We attribute the formation of W/R[E] (Figure 2, red dots) to the large volume difference between the resin and water phases, with the resin being the dominant phase, with the R/W[E] forming for a similar reason (Figure 2, magenta dots). When the resin/water mass ratio decreased below 1.0, R/W[CE] structures were observed (Figure 2, green dots). Of note, increasing the loading of GO is expected to increase the interfacial area of the system. As for the middle part of the morphology map, bijel structures form when the resin/water mass ratio is 1.4-1.5 or 2.2-2.3, where the water and resin phases are discrete from each other but entangled in a continuous tortuous pattern (Figure 2, yellow dots). In this region, the volume difference between the resin and water phases is small, while the GO concentration is high (i.e., there are more nanosheets in the system than needed). Therefore, forming an interpenetrated bicontinuous structure with a high interfacial area can harness more GO nanosheets and lower the overall free energy of the system in comparison with forming a general emulsion at the same water/resin ratio. In addition, during the shearing process, the high viscosity of the system and its viscoelastic solid-like behavior can kinetically trap the bicontinuous morphology, increasing the likelihood of maintaining jammed structures and preventing the rupture/collapse of the continuous domains. <sup>48,49</sup> In the combination of bijel and emulsion, a microstructure similar to the pure bijel is observed, but there are regions in which the water and resin phases are not always co-continuous (compare Figure S3, sample 10 and samples 11 and 12).

Regardless of GO concentration, similar trends in emulsion structure are observed, indicating that the structures formed are dominated by the resin/water ratio (Figure 2, compare line u with lines v–y). However, for different GO/water concentrations at the same resin/water ratios, although the microstructures are similar, the features vary (domain size, sphericity of emulsion droplets). For instance, comparing R/W[E] prepared from different GO concentrations, sample 6 shows emulsion droplets with good sphericity, while samples 14, 22, 30, and 38 are oblong (Figure 2, line F). This may be due to different viscosities of the samples derived from different GO loadings, where the resin droplets are unable to rely on interfacial tension to achieve a spherical morphology in more viscous system because of the high yield stress of the system.

#### **Inkability** map

With the morphology map and an understanding of fluid-fluid phase behaviors, we then identified the compositions that can serve as DIW feedstock to produce electrically conductive structures. An ideal ink for DIW should be easily extruded from the printing nozzle, quickly recover to its original viscosity after extrusion, and hold its shape upon curing. This requires the ink to be shear thinning, where the ink viscosity decreases as shear rate increases, and the ink should show a yield stress, described by a crossover point of the storage and loss moduli. Furthermore, to have suitable rheological properties for DIW, the ink viscosity should change rapidly with the shear rate and recover to its original value as the shear is removed. <sup>50,51</sup> The extruded ink should be readily cured to maintain its structure, without delamination from neighboring printed filaments. In the GO-containing inks, the cured objects should be stable to the aqueous reduction of GO, and the reduced GO (rGO) should



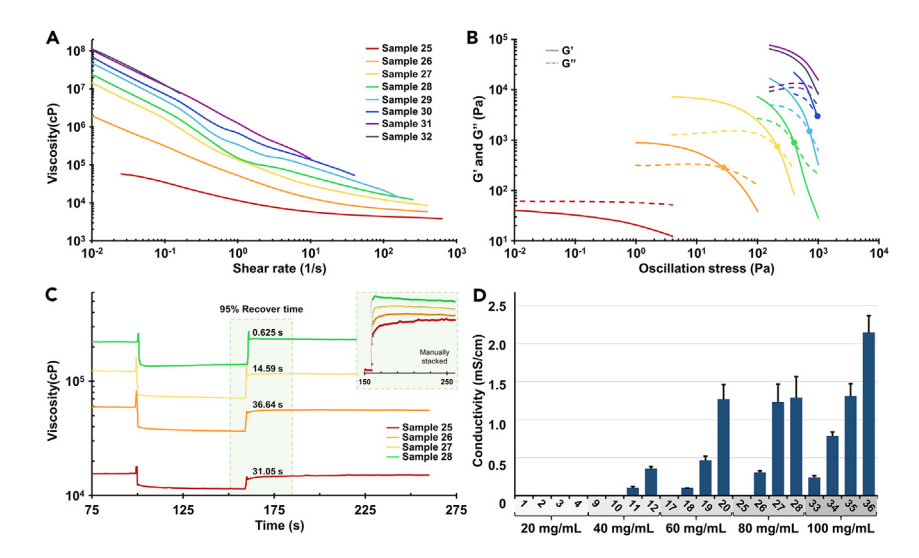


Figure 3. Inkability characterization of different compositions

Taking sample points from morphology map, line x, as an example.

- (A) Average viscosity of ink as a function of shear rate (samples 25-32).
- (B) Storage modulus (G', solid lines) and loss modulus (G'', dashed lines) as a function of oscillation stress (samples 25–32).
- (C) Three-interval thixotropy test (samples 25–28). Inset: a manually stacked, magnified image.
- (D) Conductivity calculated from four-point probe measurements. Error bars indicate standard deviation (n = 3).

maintain enough percolation through a filament and between filaments to ensure good electrical conductivity. These aspects, which we term "inkability," are all required for successful printing of conductive porous material and thus encourage an inkability map to be produced.

Viscosity test results for all sample formulations can be found in Figures 3A and S4-S6. The as-received photocurable resin is a Newtonian fluid, where the viscosity does not change with shear rate. However, when GO/water dispersion was introduced into the ink, all formulations along the morphology map were found to possess shear-thinning behavior (viscosity decreased with increased shear rate), demonstrating potential for 3D printing. For low GO loadings, no notable differences in viscosity between samples are observed (compare Figures S4A and S4B). This can be attributed to the high loading (>70.0 wt %) of the Newtonian resin and low loading of GO ( $\leq$  2.0 wt %). Generally, increasing GO wt % in the system increases the composite viscosity and extent of shear-thinning behavior (i.e., negative slope of the viscosity-shear rate curve), as expected based on the viscosity-shear rate curves for pure GO/water dispersions shown in Figure S7. This is observed for composites with a resin/water ratio that is constant (Figures S4C-S4H) or decreasing (Figures 3A and S5). Notably, for samples with resin/water ratios below 1.5, the viscosity-shear rate curves overlap with each other (e.g., Figure S4F, samples 22, 30, 38, R/W[E]). This may be due to the high loading of nanosheets that leads to high viscosities, which makes the shear thinning behavior of the inks difficult to differentiate from each other. As shown in Figures S5A and S5B, for samples with the same GO/water concentration, no proportional relationship between the viscosity and increasing GO wt % is observed, nor for decreasing resin/water mass ratio, which may be due to the low wt % of GO particles not imparting shear-thinning behavior as expected (increasing the particle wt % of the whole system leads to stronger shear-thinning behavior).





To evaluate yielding behavior of the inks, stress amplitude sweeps were performed, and the storage (G') and loss (G") moduli are plotted against stress amplitude (Figures 3B and S8-S10). For samples with resin/water mass ratios that are constant (Figure S8) or decreasing (Figures 3B and S9), increasing GO wt % of the system led to increased values of the yield stress and modulus. At lower or higher GO concentration, a yield point cannot be observed. For example, among samples 25–32 (Figures 2, line x, 3B, and S10), only samples 26-30 (sample 26, W/R[E]+[B]; sample 27, [B]; sample, 28 [B]; sample 29, R/W[CE]; and sample 30, R/W[E]) have yield points. Sample 25, a W/R[E], exhibits viscous behavior across all stress amplitudes, with G'' > G', but samples 31 and 32, both R/W[E], are dominated by elastic behavior, with G' > G'' throughout the testing range, and a yield point was not observed. Notably, for samples 1-8 (Figure S9A) and 9-16 (Figure S9B), the trend of the yield stress is staggered (yield points do not follow the expected trend of higher GO loading, leading to higher yield stress at a controlled water/resin ratio); again, this may be because lower loading of nanosheets is not enough to control the samples to show the expected yield stress trend. Characterization of aqueous dispersions of GO reveals that G', G", and yield stress increase with increasing nanosheet concentration (Figure S11). This supports that the GO nanosheets modify the rheological properties of the system, in addition to serving as a particle surfactant.

The recovery of the sample viscosity to its original value after being extruded from the printing nozzle, as critical for inkability, was evaluated using three-interval thixotropy tests. Samples were first held under a steady shear rate of 0.5 1/s to achieve a viscosity plateau (first stage), followed by a sudden increase in shear rate to 1.0 1/s for 1 min (second stage), and then returned to a shear rate of 0.5 1/s (third stage). Generally, high GO wt % or low resin/water ratio decreased the time required for the samples to recover more than 95% of initial viscosity values; these attributes are beneficial for DIW because extruded layers must support themselves and subsequent layers atop of them. As shown in Figures 3C and S14, samples with lower resin/water ratio and higher GO wt % (samples 25–28: sample 25, W/R[E]; sample 26, W/R [E]+[B]; sample 27, [B]; and sample 28, [B]) require less time (from 31.05 s to 0.625 s) to recover to 95% of the viscosity in the first stage. Additionally, thixotropy tests of samples with similar resin/water ratio but different GO loadings revealed that, as the GO wt % increased, the recovery time decreased (Figure S12; samples 4, 12, 20, 28, and 36; all [B]), which aligns with aqueous GO dispersions (Figure S13).

A critical characteristic of 3D printed objects is that the ink can be cured to "lock in" the printed geometries and survive additional processing. Curability tests of all compositions were carried out by drop casting the ink onto a slide, adding a cover slide with 1-mm spacers, and irradiating with UV light (Figure \$15). Successfully cured samples were identified as remaining intact after separating the slides, while unsuccessfully cured inks broke when detaching, as shown in Figure S16. Only samples along lines A-D in Figure 4 were curable, which is expected based on the microstructure of the inks, with curing of W/R[E] and [B] yielding monoliths because of the continuous resin domains (Figures 2 and 4, yellow, blue, and red dots). In contrast, curing of R/W[E] did not lead to robust foams because cross-linking only happened in the discontinuous phase (resin droplets) (e.g., Figures 2 and 4, green and magenta dots). The successfully cured objects were then immersed in an aqueous solution of ascorbic acid to reduce the GO nanosheets and, ideally, impart electrical conductivity to the object. Four-point probe resistivity measurements show that conductivity increased with increased GO wt % (Figure 3D; Table S2, wt % after water removal). Notably, conductivity is not dictated solely by loading of GO but also impacted by microstructure and pore connectivity. For example, porous structures obtained from



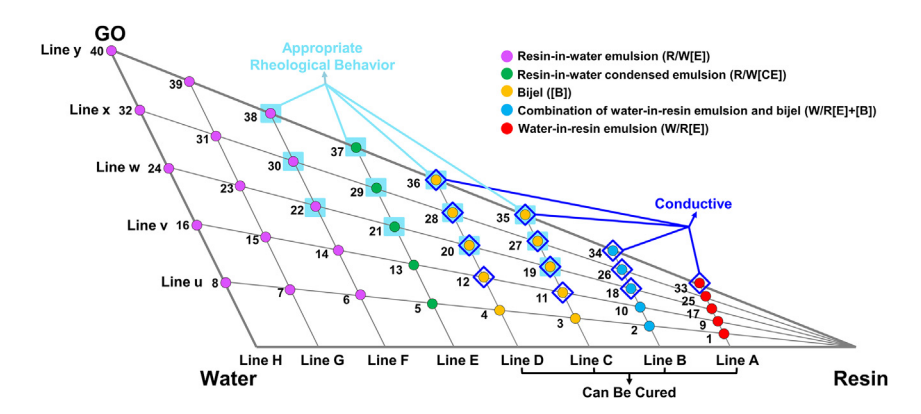


Figure 4. Inkability map

Light blue squares indicate samples with appropriate rheological behavior for DIW, lines A–D indicate samples that can be cured and maintain structure, and dark blue boxes indicate samples that have measurable conductivity (4-point probe).

bijel samples 12 and 19 show different conductivity despite having similar wt % GO. This may be attributed to differences in porosity (19.3% and 27.2%, respectively), void connectivity, and domain size, which can affect the nanosheet percolation and thus influence the bulk conductivity. By taking into account the rheological behavior, curability, and conductivity, a desired inkability map (Figure 4) with bijel samples 19, 20, 27, 28, 35, and 36 as ideal inks is obtained.

### Microstructures of foams

As described above, printed objects were immersed in an aqueous solution of ascorbic acid to reduce the GO nanosheets and impart the objects with conductivity, after which the obtained structures were dried under reduced pressure to remove water, providing porous structures that do not collapse. This is distinctly different from prevalently used freeze-drying, which requires low temperature and long drying time, and thus the drying process employed here is simple, energy and time saving, and safer. To identify the microstructure of the printed, cured, and dried objects, scanning electron microscopy (SEM) was used. The microstructure of foams dictates their physical (and thus macroscopic) properties. Only the curable morphologies were characterized by SEM, and of these, only the bijel shows good connectivity of voids. As shown in Figure 5A, for structures obtained from samples 25-28 (W/R[E], W/R[E]+[B], [B], and [B]), the structures become increasingly porous, and the domain sizes of the resin channels and void channels (i.e., previous water channels) decrease in thickness. These SEM images are consistent with the confocal fluorescence microscopy images of the corresponding inks discussed above. The W/R[E] ink, sample 25, leads to a structure that had few non-connected voids, as expected. In comparison, the SEM image of the W/R[E]+[B] sample shows more voids with some interconnected channels, again consistent with the confocal image of the corresponding ink. As for objects obtained from samples 27 ([B]) and 28 ([B]), structures with fully connected void channels are evident. For bijel samples, when the resin/water ratio is held at a similar mass ratio and GO loading is increased (Figure 2, line D), the open cells become increasingly porous, leading to interconnected voids. This can be attributed to the higher loading of GO forming finer bijel structure precursors (Figure S17). In addition to SEM imaging, a 3D structure was created to highlight the microstructure and interconnected void spaces. Figure 5B shows the 3D reconstruction from micro-X-ray computed tomography (μCT) of the printed, cured, and dried sample 20 ([B]). Interestingly, the porosity computed based on the 3D constructed model (Figure 5C) was 49.45%,



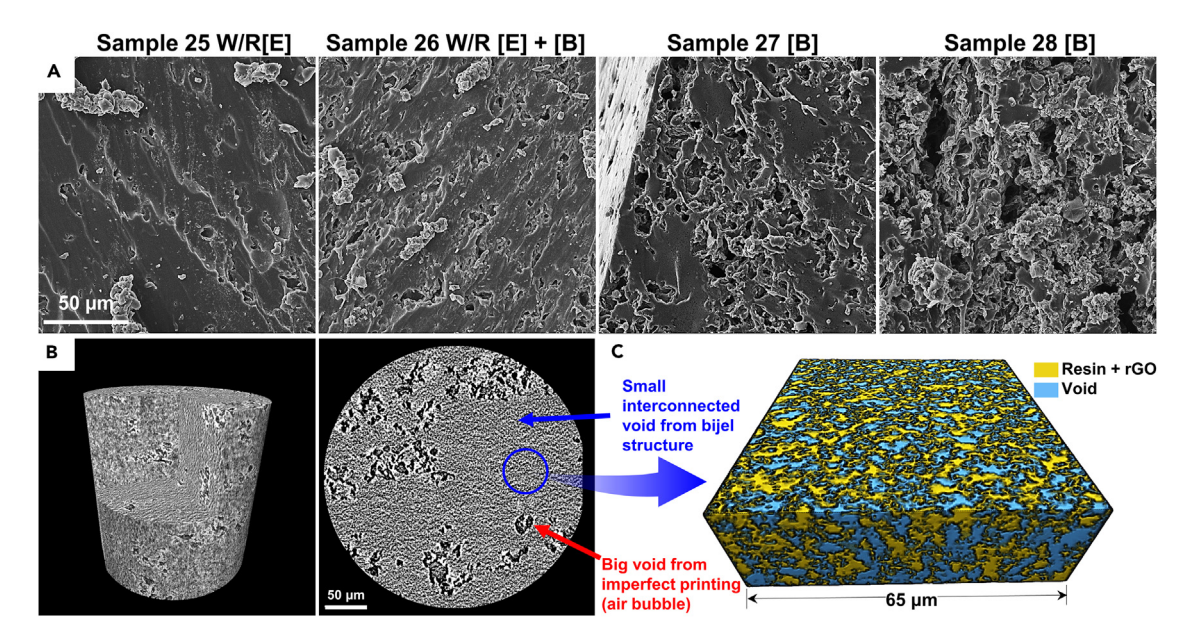


Figure 5. SEM and  $\mu$ CT characterization of selected foams

- (A) SEM images of obtained foams of samples 25–28 (corresponding to sample points in Figure 2, line x). Scale bar: 50 µm.
- (B)  $\mu CT$  of a 3D-printed structure of sample 20. Scale bar: 50  $\mu m.$
- (C) Reconstructed model of a slice of the  $\mu CT$  image shown in (B).

which is larger than the theoretical porosity (34.7%, see next paragraph). This can be attributed to the fact that the rGO flakes, constrained at the resin/air interface, were not properly assigned as part of the skeleton. The contrast in  $\mu$ CT images largely depends on the ability to impede X-ray penetration, where the low-density rGO flakes at the resin/air interface may produce poor contrast in the obtained images. This can lead to the nanoparticles being calculated as voids (air), which would consequently result in an overestimation of porosity.

In complement to the imaging of porosity and void interconnectivity afforded by SEM and  $\mu$ CT, we also measured the void space of the structures by comparing bulk density and skeletal density. Here, the bulk density was calculated through the ratio of the object's mass and volume, and skeletal density was obtained using the ethanol immersion method, as detailed under experimental procedures. Table S3 summarizes the density and porosity data. In line with the SEM images, the porosity from samples 25–28 (Figure 2, line x) does increase (1.59%–35.8%), and density shows a correspondingly decreasing trend (1.11 g/cm³ to 0.72 g/cm³). Additionally, foams obtained from bijels (Figure 2, line D) with similar resin/water ratios increase in porosity (10.4%–42.9%) with increased GO loading, with density decreasing concurrently (1.01 g/cm³ to 0.64 g/cm³), which is aligned with the SEM images shown in Figure S17. The calculated result from the ethanol immersion method is only slightly lower than the theoretical value. This deviation is because ethanol may not fully wet the voids trapped in the aforementioned rGO flakes, thus leading to a lower calculated porosity.

# **Mechanical performance**

Mechanical performance is important for most applications, including wearable materials, because the printed structures should show excellent tolerance to being stretched, twisted, and compressed. The microstructure of a porous object plays a critical role in tuning the tensile performance. The Young's moduli (E) of the reduced and unreduced open-cell foams from sample 12 ([B]; Figure S18) support that



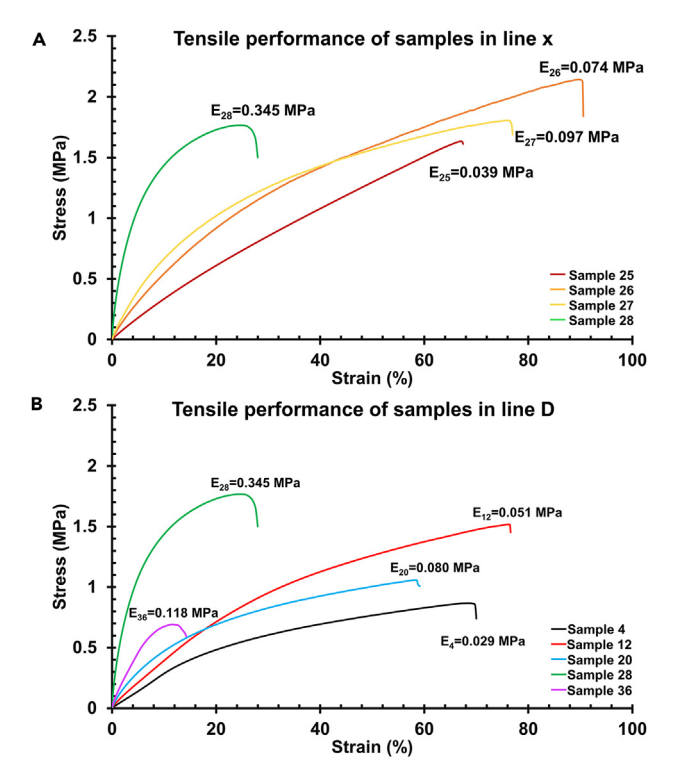


Figure 6. Representative stress-strain curves of foams made from samples

(A) Same GO/water concentration, increasing GO wt % as shown in Figure 2, line x.

(B) Similar resin/water mass ratio and increasing GO wt % as shown in Figure 2, line D.

ascorbic acid treatment does not have a notable impact (E is 0.05 MPa and 0.04 MPa, respectively). However, the unreduced sample shows larger uniform strain under similar ultimate stress. We then compared the E of the foams from different morphologies (e.g., W/R[E] and W/R[E]+[B]). From samples 25–28 (sample 25, W/R[E]; sample 26, W/R[E]+[B]; sample 27, [B]; and sample 28, [B]), increasing elastic modulus values are observed (Figure 6A). This is due to a combination of decreased elastic resin content, increased porosity, and increased particle filler loading, all factors that increase the stiffness of the samples. For the open-cell foam (all [B]), increasing GO wt % led to increasing E (Figure 6B). This further supports that increasing particle filler loading and porosity make the material stiffer. Notably, sample 36 has higher GO loading, higher porosity, and a lower amount of elastic resin compared with sample 28; however, its elastic modulus is slightly lower compared with sample 28. This may be due to the high loading of the nanosheets inducing particle aggregation, which lowers the effective surface area of particles to hinder polymer chain mobility. 52,53 In comparison with graphene/elastomer composites prepared by other prevalently used methods (e.g., solution blending, nanoparticle infiltration) and other polymer identities (e.g., polydimethylsiloxane, TPU), the bijel-templated graphene/resin structure reported here has a lower Young's modulus. In addition, the material demonstrates larger elongation (percent) at break (58.7% versus <50% in other recent reports) and thus shows superior ductility (Table S4), which is significant for application in wearable devices.

# 3D printing of inks and wearable materials

Bijel inks (samples 20 and 28) that yielded electrically conductive structures were printed into cubic lattices through different-sized nozzles. As shown in



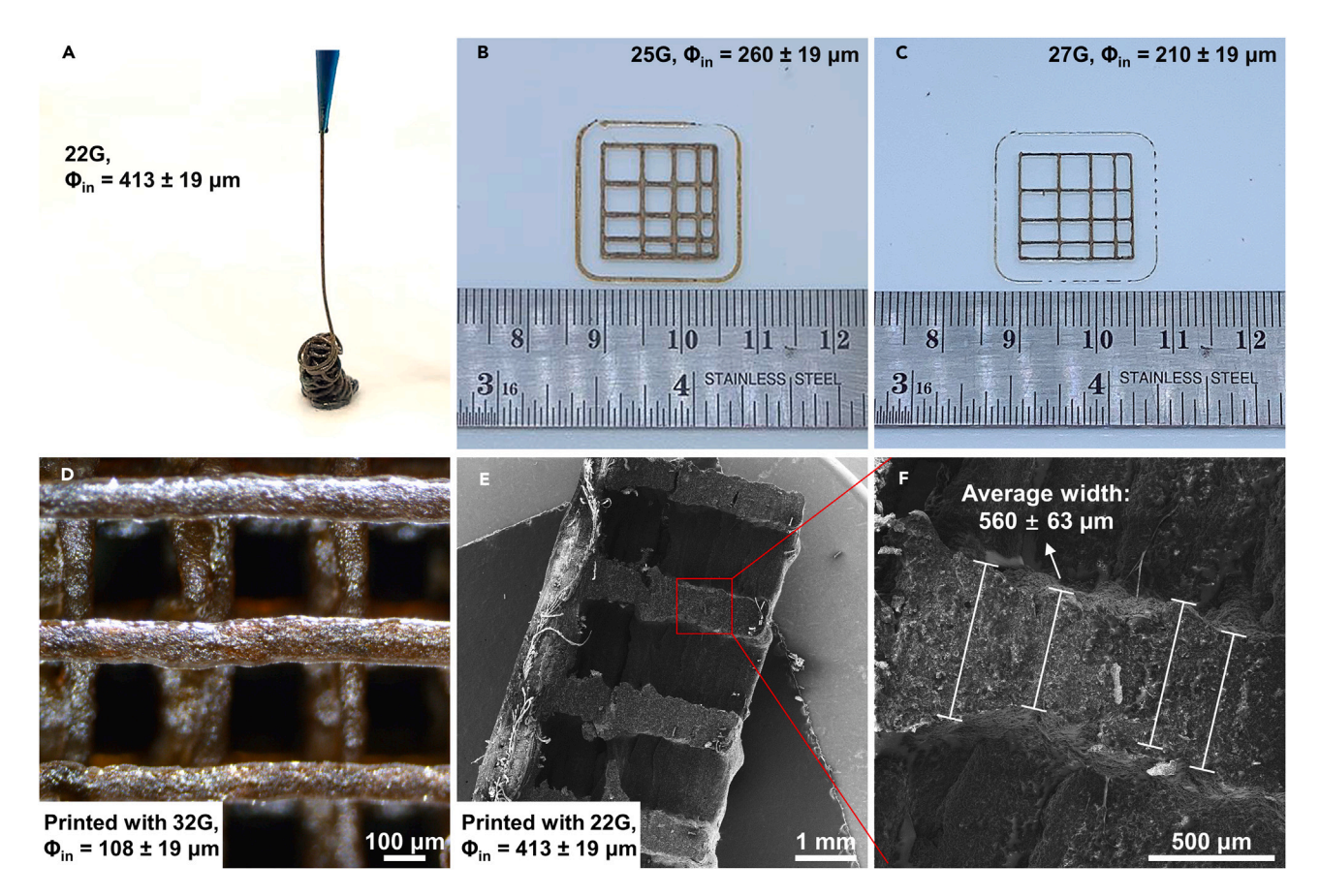


Figure 7. Printing resolution and fidelity tests

(A–D) Printing resolution test and digital images of printed cubic lattice; in (A)–(C), sample 28 was used, and (D), sample 20 was used (scale bars:  $100 \, \mu m$ ). (E and F) SEM images of a cross-section of a printed cubic lattice from sample 28. Scale bars are 1 mm and  $500 \, \mu m$ , respectively.

Figures 7A–7C, sample 28 can be readily extruded and printed with 22G, 25G, and 27G nozzles ( $\phi_{in}\sim$ 413,  $\sim$ 260, and  $\sim$ 210  $\mu m$ , respectively). Subsequently, cubic lattices were printed with nozzle  $\phi_{in}$  of 260  $\mu m$  (25G) and 210  $\mu m$  (27G); even with the 27G nozzle, the outline of the smallest square (2.0  $\times$  2.0 mm) in the printed cubic lattice can be seen clearly, which indicates high print fidelity and potential applications in high-resolution printing. Because sample 20 possessed a lower viscosity compared with sample 28, it should be printable using a smaller-diameter nozzle; Figure 7D shows an optical microscopy image of a cubic lattice printed from sample 20 using a 32G nozzle (( $\phi_{in}$  = 108  $\pm$  19  $\mu$ m), demonstrating that higher-resolution structures can be obtained by using a lower-viscosity ink. SEM characterization of a cross-section of the printed cubic lattice of sample 28 using a 22G needle indicates that adjacent filaments of the ink can be clearly distinguished and do not merge or spread significantly during printing (Figures 7E and 7F). Notably, the filament width (560  $\pm$  63  $\mu$ m) is slightly larger than the nozzle inner diameter (413  $\pm$  19  $\mu$ m), which is due to the die swell effect.

For wearable applications, inks should be printed onto clothing materials, such as fabrics, and therefore must have excellent adherence. As shown in Figure 8, printing sample 28 ([B]) onto 100% cotton Aida cloth gave good fidelity, with the structure having excellent flexibility, and it is able to be stretched and compressed without detriment to the printed pattern (Figures 8A and 8B). Notably, neither the mild conditions used to reduce the GO nanosheets (i.e., ascorbic acid) nor removal of water



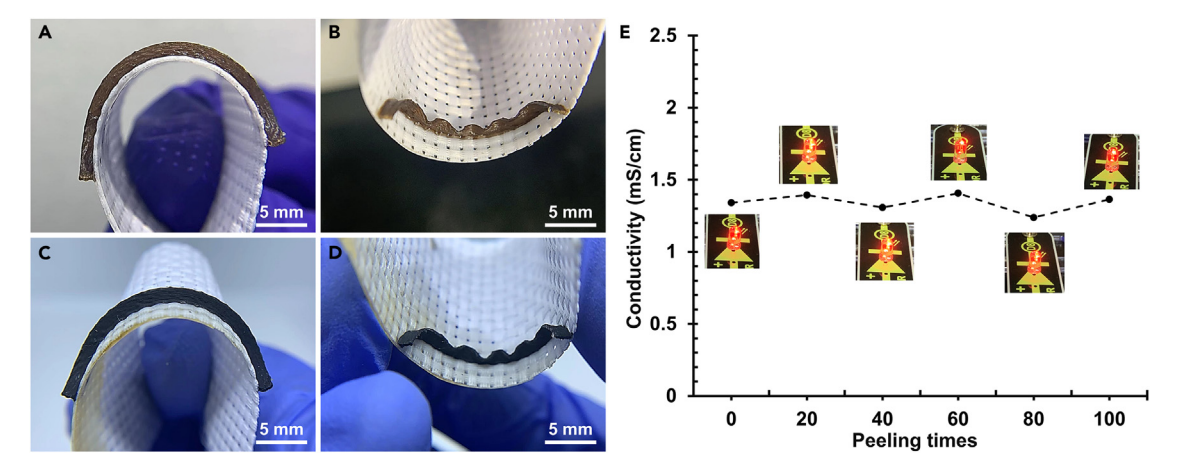


Figure 8. Flexibility and adhesiveness tests

(A–D) Printed sample 28 and flexibility test of printed samples before (A and B) and after (C and D) treatment with ascorbic acid and vacuum drying. Scale bars: 5 mm.

(E) Conductivity as a function of number of peels, as determined by four-point probe measurements. Pictures of light bulbs show that the printed foam still can be used to connect a circuit after the peeling test.

impacted the adhesion or flexibility of the printed objects (Figures 8C and 8D), demonstrating the robustness of the system. To further understand the adhesivity of the printed material to the fabric, a cuboid pattern (i.e., a cubic lattice with 100% infill) was printed onto the cloth, processed, and then subjected to a peel test, where packing tape was applied to the top of the cuboid and then peeled off, with the conductivity tested after every 20th round of peeling. Figure 8E shows that the conductivity of the structure remained nearly constant at ~1.3 mS/cm after peeling more than 100 times (an illustration of a circuit for a light bulb-lighting test is shown in Figure S19), confirming that the printed structure maintains its integrity and adherence to the cloth substrate. Figure S20 shows that more complicated structures can also be printed onto the same fabric. The amphipathic nature of bijel, because of a combination of water and resin channels, gives the ink good affinity for hydrophilic and lipophilic fabrics. Figure S21 shows that the ink can be successfully printed onto 100% cotton and 50/50 cotton/polyester fabric materials reduced with ascorbic acid and dried under vacuum without delamination.

# Radio frequency heating

Printed objects with continuous and connected void structures that have appropriate conductivity are expected to have excellent radio frequency (RF) heating performance, which can be promising for applications such as packaging, sanitation, and material curing/sintering. 54-56 Figure 9A demonstrates the RF heating test setup, and Figure 9B shows the frequency sweep result, where heating rate is plotted as a function of radiation frequency. A maximum heating response at around 125 MHz was observed, which was used for all subsequent tests. As shown in Figure 9C, an RF heating cycle was performed at 125 MHz and 1 W power for five different structures obtained from bijel inks (different GO wt % but similar resin/water ratios). For all samples, rapid heating was observed within 1.0 s of exposure to low-power RF. Interestingly, with a similar resin/water ratio bijel precursor, the heating response of the obtained porous structures first increased and then decreased with increasing GO loading, giving sample 20 (4.0 wt % of GO of obtained foam) the highest heating response by reaching 240.7°C within 0.92 s. This trend can be attributed to the electrical conductivity and the microstructure of the samples. Specifically, less conductive samples (e.g., samples 4 and 12) do not sufficiently absorb





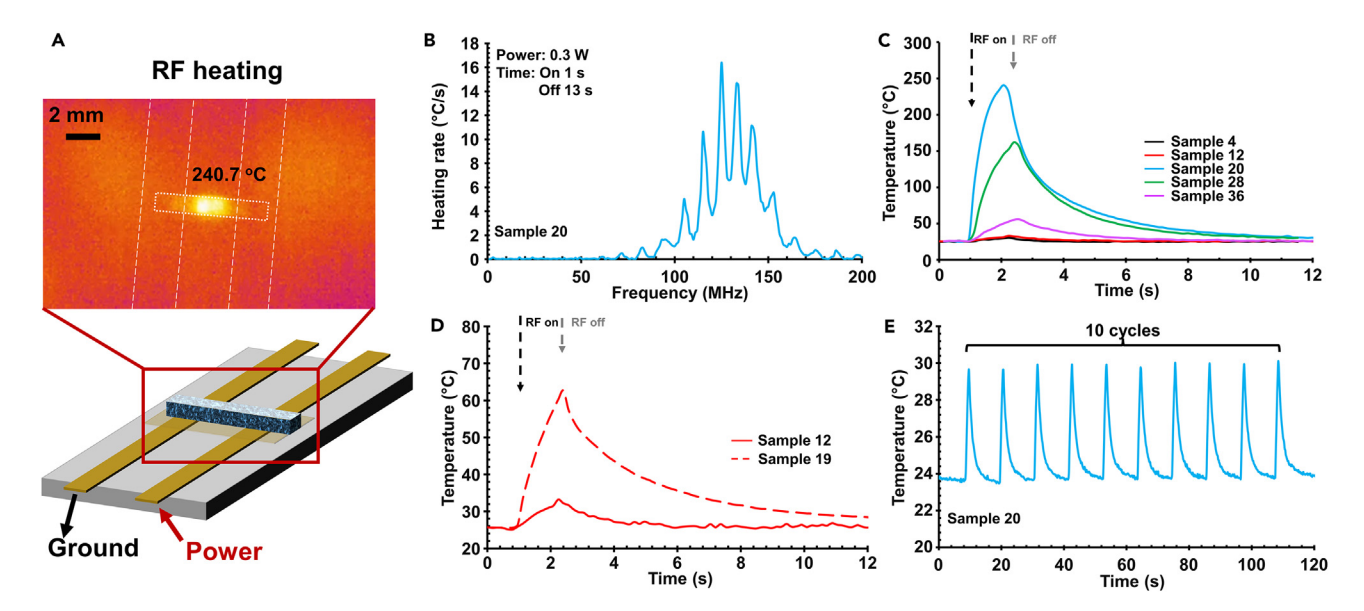


Figure 9. RF heating performance of selected foams

- (A) Schematic of the RF heating test setup. Scale bars: 2 mm.
- (B) Frequency sweep of sample 20 varied from 1-200 MHz.
- (C and D) RF heating of foams at 125 MHz at 1 W.
- (E) Cyclic heating test of sample 20 upon exposure to 125 MHz at 0.1 W.

the EM wave, while those with a highly conductive network (e.g., sample 36) reflect the EM wave and consequently reduce the heating response. To further define the impact of microstructure on heating response to EM waves, foams obtained from bijel samples 12 and 19 with a similar GO loading (2.7 wt % and 2.6 wt %) but different porosities (19.3% and 27.2%) were exposed to an RF field. As shown in Figure 9D, sample 19 gave a more rapid and intense temperature response compared with sample 12, confirming that the microstructure (void channels) directly impacts the RF heating response, where higher void space leads to a more rapid and intense heating response. A similar temperature change is observed over 10 RF heating cycles, indicating good stability of the sample (Figure 9E). Of note, as shown in Table S5, the open-cell foam templated by the bijel structure shows a much faster response to RF at a lower nanosheet loading compared with previously reported particle/polymer composites.

# Applicability to other particle systems

The proposed methodology provides a roadmap of preparing 3D printable and wearable conductors from bijel-based inks, provided conductive particle surfactants or their precursors can be used. We thus evaluated whether the morphology map developed above can guide the micromorphology of printed objects using transition metal carbide nanosheets (i.e., MXene) in place of GO nanosheets. Specifically, a  $Ti_3C_2T_z$ -GO system was used to produce analogs of sample 4 ([B]), sample 7 (R/W [E]), sample 20 ([B]), and sample 23 (R/W[E]), with the expected phase behaviors successfully obtained for each system. Similar to GO, MXenes can act as solid stabilizers (e.g., Pickering surfactant) for fluid-fluid interfaces,  $^{57,58}$  with the added benefit that MXenes themselves are conductive, thus removing the need for chemical reduction as required for GO. As shown in Figure S22, different inks were readily prepared using a mixture of MXene and GO (wt:wt = 3:1), where the resin, water, and overall particle wt % were all kept the same as in the GO-only systems. Notably, MXenes cannot be used as the sole nanosheets to stabilize bijels, which we attribute



to their higher hydrophilicity than GO (e.g., negatively charged faces of the nanosheets). Comparison of the confocal fluorescence microscopy images of the GO-only and  ${\rm Ti_3C_2T_z}$ -GO systems reveals that similar microstructures are produced for each phase identified in the morphology map (i.e., R/W[E], [B], etc.). Thus, the morphology map produced here can be used to guide bijel formation with other functional 2D particle systems or immiscible fluid systems to produce inks tailored for specific applications.

#### **Conclusions**

Here we developed a platform to produce 3D-printable ultralight conductive foams with continuous voids via the construction of a morphology map of water, resin, and 2D GO particle surfactants. Composition-dependent ink optimization was used to define the morphology, rheological properties, and curability of the systems as well as the microstructure and electrical conductivity of the printed structures. Six ink compositions were identified as ideal for producing 3D-printable, conductive, low-density structures, all of which are bicontinuous emulsions (i.e., bijels) and have a resin/water mass ratio at 1.4-1.5 with 4.0-6.7 wt % nanosheets or at 2.2-2.3 with 2.5-4.3 wt % nanosheets. Extrusion-based DIW printing of the inks, followed by UV curing of the resin phase, ascorbic acid reduction of the GO nanosheets, and drying under reduced pressure yielded ductile foams with continuous void space throughout the polymer matrix. The structures of the printed objects and interpenetrated channels were characterized by SEM, µCT, and density measurements. Compared with traditional techniques, utilization of bijel ink avoids complicated, energy-consuming processing procedures such as gas-foaming agent injection, freeze-drying, acid etching, sintering, and template removal, during the preparation of the porous structure. In the bijel system reported here, removal of the water phase yields a continuous void phase with a percolation of the conductive particles. The bicontinuous morphology also quarantees the high interconnectivity of the void channels that is required for energy/mass transport and percolation of the conductive fillers that general emulsion morphology may not be able to achieve. In addition, the entangled structure of the hydrophobic phase (resin) and hydrophilic phase (water) imparts the ink with excellent penetration of substrates with different wettability, which is indispensable for mass production and adaptability of wearable devices.

Characterization of electrical conductivity, mechanical properties, and adhesiveness to fabric of the printed bijels underscores the important complementarity of composition and structure on performance-related properties. Compared with other prevalently reported graphene/polymer composites, our materials present a lower Young's modulus and a larger elongation percentage at break, which indicates excellent ductility. Further RF heating experiments showed that the open-cell foams with only 4.0 wt % nanosheet loading exhibit an extremely rapid response to EM waves within 1.0 s, demonstrating a much better performance in rapid RF heating compared with previously reported particle/polymer composites.

The system developed here provides critical insights into how to leverage fluid-fluid phase-separated systems and 2D particle surfactants for the development of next-generation composites. This paradigm shift gives access to bicontinuous emulsions for use as inks with minimal pre/post-processing requirements to produce ultralight conductive materials with good adhesion to fabrics and, thus, suitability for wearable applications. Additionally, we demonstrate that this morphology map-guided ink development can also be applied to other 2D particle systems; namely, MXenes. Bijel inks for DIW not only broaden the scope of 3D printing of emulsion-based inks but also take advantage of the biphasic structures to pave the way for defining





composition-microstructure relationships. Indeed, these emulsion-based inks open exciting possibilities for using the macroscopic geometry afforded by print and microscopic porosity afforded by ink formulation to tailor performance-related properties for a number of applications.

#### **EXPERIMENTAL PROCEDURES**

### **Resource** availability

#### Lead contact

Further information and requests for resources and reagents should be directed to and will be fulfilled by the lead contact, Peiran Wei (peiran@tamu.edu).

#### Materials availability

This study did not generate new unique reagents.

#### Data and code availability

This study did not generate datasets.

#### **Materials**

Photocurable Elastic 50A resin was ordered from Formlabs (part number RS-F2-ELCL-01). Aqueous hydrogen peroxide ( $H_2O_2$ ; 30% [w/w]), ethanol (99.5%), and isopropanol ( $\geq$ 99.5%) were purchased from Fisher Scientific. Graphite flakes, sulfuric acid ( $H_2SO_4$ ), and potassium permanganate (KmnO<sub>4</sub>;  $\geq$  99%) were bought from Sigma-Aldrich. All chemicals were used as received. Ti<sub>3</sub>AlC<sub>2</sub> MAX phase was prepared as reported previously. <sup>59,60</sup> 50/50 cotton/polyester fabric and 100% cotton fabric were purchased from Walmart, and 100% cotton Aida fabric was purchased from Amazon (manufacturer: Similane).

#### Instrumentation

Emulsification (ink formation) was realized by a conditioning mixer from Thinky (model AR-100). Sonication was done through an ultrasonic bath (model CPX 3800), and vortexing was accomplished by a vortex mixer (model 9454FIALUS); both were from Fisherbrand. Centrifugation was performed with a SORVALL ST 8 centrifuge (Thermo Fisher Scientific). Blending of GO flakes was achieved by a Waring commercial blender (model 7010S). Optical microscopy images were taken using an AmScope 150C-2L microscope with an 18 MP USB 3.0 camera. Confocal fluorescence microscopy images were taken with an Olympus FV 1000 confocal platform at 405-nm excitation wavelength. SEM images were taken with a Tescan Vega SEM. Optical images of the printed inks and printed objects were recorded using an iPhone X. Rheological properties were analyzed using a TA Instruments DHR-2 rheometer with a 40-mm parallel plate. Mechanical properties were measured with a TA Instruments DMA 850 with a film clamp. The direct current (DC) conductivity was obtained using a standard Keithley 4-point probe meter. The 3D printing was performed on a Hyrel 3D Engine SR with an SDS-10 syringe extrusion head. μCT was done on an Xradia 520 Versa (XRM, Carl Zeiss) X-ray microscope. The RF fields were generated using a RIGOL DSG815 signal generator and then amplified using a PRANA GN 500 power amplifier.

## Synthesis of GO

GO was synthesized through the oxidation of graphite flakes following a previously reported modified Hummer's method.  $^{61}$  In brief, graphite flakes (3.0 g) were mixed with  $H_2SO_4$  (400 mL) followed by the addition of 3.0 g KMnO<sub>4</sub>. The reaction was kept at room temperature with magnetic stirring and another three batches of KMnO<sub>4</sub> (3.0 g per batch) were added to the mixture at 24-h intervals. The reaction was quenched by pouring the resulting purple suspension into ice water (2.0 L), followed



by the dropwise addition of aqueous  $H_2O_2$  (30%) until the color turned to light brown. The product was washed with isopropanol until the pH reached approximately neutral. The final product was dried under reduced pressure, blended into powder, and stored at  $2^{\circ}C-8^{\circ}C$ .

## Ink preparation

The inks were composed of water, resin, and GO, with compositions of different ink identities listed in Table S1. First, GO powder was dispersed in water in a glass vial to form a GO/water dispersion with the assistance of vortex mixing and sonication. Resin was then charged into the same vial, followed by homogenization using a Thinky mixer at a mixing speed of 400 rpm for 1 min. Next, the formed ink was vortexed for 20 s, followed by defoaming using the Thinky mixer for 30 s at the fixed speed inner-set by the mixer.

## Rheometry

All rheological experiments were performed on a rotational rheometer with a 40-mm parallel plate at  $25^{\circ}\text{C}$  with the gap distance set to  $500~\mu\text{m}$ . The viscosity of each ink was measured three times over shear rates from 0.001–1,000~Hz. A stress amplitude sweep was performed on each ink three times from 0.001–1,000~Pa at a frequency of 1 Hz, from which storage and loss moduli were measured. Three-interval thixotropy tests were carried out with a three-step shear rate changing process, where the shear rate was first held at 0.5~Hz for a few min until the viscosity curve reached a plateau, followed by an increase in shear rate to 1.0~Hz, which was held for 1~min, and then the shear rate decreased to 0.5~Hz and was held for 3~min, with each identity tested 3~times.

# 3D printing

The ink was loaded into a 10-mL Luer-Lok syringe with a dispensing needle (20G, 22G, 25G, 27G, and 32G), followed by inserting the syringe into an extrusion cartridge attached to the 3D printer. Cubic lattices were printed with desired heights and infill percentages. During the printing process, each printed layer was cured by irradiation with a 365-nm Hyrel UV Pen. The printing parameters (taking the sample shown in Figure 7B as an example) are were as follows: nozzle temperature, 22°C; layer height, 0.130 mm; number of vertical shells, 1; number of horizontal shells, 0; infill density, 100%; infill pattern, rectilinear; and infill speed, first layer speed, and travel speed, 20 mm/s.

# GO reduction and porous structure preparation

The as-prepared printed composites were immersed in an aqueous ascorbic acid solution (0.24 g/mL, 70°C) overnight to reduce the GO, followed by washing with distilled water for 5 min. The composites were dried at room temperature under reduced pressure (0.31 torr) to remove the water and produce the porous conductive structures.

#### **Density and porosity test**

The bulk density of porous structures was obtained through calculation by

$$\rho_{bulk} = \frac{m_{sample}}{V_{sample}}$$
 (Equation 1)

of a 10  $\times$  10  $\times$  0.3-mm sample piece.

Skeletal density of porous structures was estimated by an alcohol immersion method using a  $10 \times 10 \times 0.3$ -mm sample piece based on Archimedes' principle as illustrated in the literature:  $^{62}$ 





$$\rho_{\text{skeleton}} = \frac{m_{\text{sample}} \times \rho_{\text{ethanol}}}{m_{\text{sample}} - m_{\text{suspended}}}$$
 (Equation 2)

where  $m_{sample}$  and  $m_{suspended}$  stand for the dry sample mass and mass of the sample suspended in 200-proof ethanol, respectively, and  $\rho_{ethanol}$  means the density of the ethanol.

Overall porosity was calculated through

$$P_{overall} = 1 - \left(\frac{\rho_{bulk}}{\rho_{skeleton}}\right)$$
 (Equation 3)

#### **Tensile tests**

Tensile test samples of the inks were prepared through molding the ink into thin films ( $\sim$ 0.3 mm) using two glass substrates, curing them with UV radiation, and removing them from the mold. Strips approximately 2 mm in width were then cut and loaded into the film clamp of the DMA instrument. The test was performed employing a strain rate of 50% per minute.

#### **Peeling test**

A 5  $\times$  10  $\times$  5-mm cubic lattice was printed on fabric using sample 28, followed by reduction of GO through the method mentioned under GO reduction and porous structure preparation. Scotch Sure Start shipping packaging tape was applied atop the printed structure, firmly pressed down, and then peeled off. This was repeated 100 times, with the conductivity of the structure tested via four-point probe after each 20 peels (a new piece of tape was used every 20 peels).

# Four-point probe test

Test samples were prepared through molding the ink into thin foams ( $\sim$ 0.3 mm) using two glass substrates. As shown in Figure S15, the foams were then cured under UV radiation and removed from the mold. The sample was put on the testing plate with the probe inserted into the sample. The applied current was controlled at 1  $\mu$ A, and voltage data were collected to calculate the conductivity.

# **SEM** sample preparation

Small pieces ( $5.0 \times 2.0 \times 0.3$  mm) of the cured foams or 3D-printed cubic lattice ( $10.0 \times 2.5 \times 3.5$  mm) shown in Figures S20C and S20D were cut and mounted onto SEM stubs (Ø 12.7  $\times$  8 mm pin height) using conductive double-sided tape without sputter coating.

# μCΤ

A 10  $\times$  2-mm cubic lattice of sample 20 with 100% infill was 3D printed, and 2D cross-section scanning was performed through the X-ray microscope. By reconstruction of the 2D-scanned images, 3D views of the samples were successfully obtained. The experiment was carried out at atmospheric pressure and room temperature using an X-ray microscope with 80-kV voltage, 7-W power, a 360° rotation step with 1,601 projections, and 0.34- $\mu$ m voxel size. The 3D visualization of the studied specimen was realized through software reconstruction.

## RF heating

A co-planar, stationary RF applicator was used to apply the RF fields. The RF fields were produced using a signal generator and then amplified using a power amplifier. A sample with in-plane dimensions of  $5 \times 2$  mm was exposed to RF fields, and the temperature changes were recorded using a thermal camera (FLIR Systems, A655sc). For a frequency sweep test, sample 20 was exposed to frequencies ranging



from  $1-200\,\text{MHz}$  at  $0.3\,\text{W}$  with a heating time of 1 s at each frequency and then off for 13 s. For the cyclic heating test, sample 20 was exposed to an on-and-off RF heating cycle at 125 MHz and 0.1 W, repeated across 10 cycles. For the remaining heating tests, all samples were exposed to 125 MHz at 1 W for 1 s.

#### **SUPPLEMENTAL INFORMATION**

Supplemental information can be found online at https://doi.org/10.1016/j.matt. 2023.10.001.

#### **ACKNOWLEDGMENTS**

The authors thank the NSF for DMR grant 2103182 and Texas A&M University for financial support. C.C. acknowledges the NASA Space Technology Graduate Research Opportunity. The authors acknowledge use of the Soft Matter Facility and Microscopy and Imaging Center at Texas A&M University. The authors acknowledge Mr. Oscar Huang for guidance regarding the ethanol immersion method. The authors acknowledge Dr. Kailu Xiao for guidance regarding porosity calculation. The authors acknowledge Dr. Justin Smolen and the Karen Wooley group for confocal microscopy. The authors also acknowledge Mr. Ethan Hammond for helping with the graphene oxide synthesis.

#### **AUTHOR CONTRIBUTIONS**

E.B.P. and P.W. conceptualized and supervised the project. P.W. and Y.W. designed the experiments. Y.W. carried out all laboratory experiments and data analyses under the guidance of P.W. C.C. assisted with initial experimental trials. C.-M.H. assisted with 3D printing. H.C. provided MXenes and assisted with four-point probe testing. Z.T. provided MAX phase under the guidance of M.R. A.S. and M.J.G. helped with the RF heating test. K.-W.L. assisted with CT scanning. Y.W. and P.W. wrote the initial manuscript. All authors discussed the results and contributed to the final manuscript. All authors have given approval to the final version of the manuscript.

## **DECLARATION OF INTERESTS**

The authors declare no competing interests.

Received: February 15, 2023 Revised: June 5, 2023 Accepted: October 2, 2023 Published: November 1, 2023

### **REFERENCES**

- Zhai, T., Li, D., Fei, G., and Xia, H. (2015). Piezoresistive and compression resistance relaxation behavior of water blown carbon nanotube/polyurethane composite foam. Compos. Appl. Sci. Manuf. 72, 108–114. https://doi.org/10.1016/j.compositesa.2015. 02.003.
- Zhou, K., Dai, K., Liu, C., and Shen, C. (2020). Flexible conductive polymer composites for smart wearable strain sensors. SmartMat 1, e1010. https://doi.org/ 10.1002/smm2.1010.
- Lage-Rivera, S., Ares-Pernas, A., and Abad, M.J. (2022). Last developments in polymers for wearable energy storage devices. Int. J. Energy Res. 46, 10475–10498. https://doi.org/10.1002/ er.7934.
- Wu, G., Du, H., Lee, D., Kim, W., Cha, Y., Zhang, X., and Kim, D.-J. (2022). In Wearable Conductive Polymer Matrix Composites for Breath Monitoring with Ammonia Detection, 62Wearable Conductive Polymer Matrix Composites for Breath Monitoring with Ammonia Detection (The Electrochemical Society, Inc.)), p. 2284.
- Kruželák, J., Kvasničáková, A., Hložeková, K., and Hudec, I. (2021). Progress in polymers and polymer composites used as efficient materials for EMI shielding. Nanoscale Adv. 3, 123–172. https://doi.org/10.1039/DONA00760A.
- 6. Wang, L., Li, N., Zhang, Y., Di, P., Li, M., Lu, M., Liu, K., Li, Z., Ren, J., Zhang, L., and Wan, P. (2022). Flexible multiresponse-actuated nacrelike MXene nanocomposite for wearable

- human-machine interfacing. Matter 5, 3417–3431. https://doi.org/10.1016/j.matt.2022. 06.052.
- Wang, Y., Liu, J., Wu, H., Cai, Y., Dai, K., Liu, C., and Shen, C. (2018). Flexible electrically resistive-type strain sensors based on reduced graphene oxide-decorated electrospun polymer fibrous mats for human motion monitoring. Carbon 12, 360–368. https://doi.org/10.1016/j.carbon. 2017.10.034.
- Wang, Y., Jia, Y., Zhou, Y., Wang, Y., Zheng, G., Dai, K., Liu, C., and Shen, C. (2018). Ultra-stretchable, sensitive and durable strain sensors based on polydopamine encapsulated carbon nanotubes/elastic bands. J. Mater. Chem. C





- Mater. 6, 8160–8170. https://doi.org/10.1039/C8TC02702A.
- Bian, Y., and Li, Y. (2022). Porous conductive elastomeric composites with carbon nanotubes suspended in the narrow pores from Co-continuous polymer blend nanocomposites. Compos. Sci. Technol. 218, 109116. https://doi.org/10.1016/j. compscitech.2021.109116.
- Chen, J., Liao, X., Li, S., Wang, W., Guo, F., and Li, G. (2020). A promising strategy for efficient electromagnetic interference shielding by designing a porous double-percolated structure in MWCNT/polymer-based composites. Compos. Appl. Sci. Manuf. 138, 106059. https://doi.org/10.1016/j. compositesa.2020.106059.
- Chen, M., Duan, S., Zhang, L., Wang, Z., and Li, C. (2015). Three-dimensional porous stretchable and conductive polymer composites based on graphene networks grown by chemical vapour deposition and PEDOT: PSS coating. Chem. Commun. 51, 3169–3172. https://doi.org/10.1039/ C4CC09367D.
- Chen, Z., Ren, W., Gao, L., Liu, B., Pei, S., and Cheng, H.-M. (2011). Three-dimensional flexible and conductive interconnected graphene networks grown by chemical vapour deposition. Nat. Mater. 10, 424–428. https:// doi.org/10.1038/nmat3001.
- Suzuki, S., and Yoshimura, M. (2017). Chemical stability of graphene coated silver substrates for surface-enhanced Raman scattering. Sci. Rep. 7, 14851. https://doi.org/10.1038/s41598-017-14782-2.
- Cui, G., Bi, Z., Zhang, R., Liu, J., Yu, X., and Li, Z. (2019). A comprehensive review on graphenebased anti-corrosive coatings. Chem. Eng. J. 373, 104–121. https://doi.org/10.1016/j.cej. 2019.05.034.
- Ge, G., Cai, Y., Dong, Q., Zhang, Y., Shao, J., Huang, W., and Dong, X. (2018). A flexible pressure sensor based on rGO/polyaniline wrapped sponge with tunable sensitivity for human motion detection. Nanoscale 10, 10033–10040. https://doi.org/10.1039/ C8NR02813C.
- Wei, P., Leng, H., Chen, Q., Advincula, R.C., and Pentzer, E.B. (2019). Reprocessable 3Dprinted conductive elastomeric composite foams for strain and gas sensing. ACS Appl. Polym. Mater. 1, 885–892. https://doi.org/10. 1021/acsapm.9b00118.
- Wei, P., Bhat, G.A., Cipriani, C.E., Mohammad, H., Schoonover, K., Pentzer, E.B., and Darensbourg, D.J. (2022). 3D Printed CO2-Based Triblock Copolymers and Post-Printing Modification. Angew. Chem., Int. Ed. Engl. 61, e202208355. https://doi.org/10.1002/anie. 202208355.
- de Leon, A.C., Rodier, B.J., Bajamundi, C., Espera, A., Jr., Wei, P., Kwon, J.G., Williams, J., Ilijasic, F., Advincula, R.C., and Pentzer, E. (2018). Plastic metal-free electric motor by 3D printing of graphene-polyamide powder. ACS Appl. Energy Mater. 1, 1726–1733. https://doi. org/10.1021/acsaem.8b00240.
- 19. Xu, J., Slykas, C., Braegelman, A.S., Alvarez, K.G., Kasl, T., Boudouris, B.W., Webber, M.J.,

- Sharma, V., and Phillip, W.A. (2022). Heavy metal removal using structured sorbents 3D printed from carbon nanotube-enriched polymer solutions. Matter 5, 3432–3451. https://doi.org/10.1016/j.matt.2022.07.012.
- Wei, P., Bhat, G.A., and Darensbourg, D.J. (2023). Enabling New Approaches: Recent Advances in Processing Aliphatic Polycarbonate-Based Material. Angew. Chem. Int. Ed.e202307507 https://doi.org/10.1002/ anie.202307507.
- Cipriani, C.E., Ha, T., Martinez Defilló, O.B., Myneni, M., Wang, Y., Benjamin, C.C., Wang, J., Pentzer, E.B., and Wei, P. (2021). Structure– processing–property relationships of 3D printed porous polymeric materials. ACS Mater. Au 1, 69–80. https://doi.org/10.1021/ acsmaterialsau.1c00017.
- Lewis, J. (2006). Direct ink writing of 3D functional materials. Adv. Funct. Mater. 16, 2193–2204. https://doi.org/10.1002/adfm. 200600434.
- Chen, Q., Cao, P.F., and Advincula, R.C. (2018). Mechanically robust, ultraelastic hierarchical foam with tunable properties via 3D printing. Adv. Funct. Mater. 28, 1800631. https://doi. org/10.1002/adfm.201800631.
- Liu, Z., Guo, Y., Lian, F., Wang, K., Sun, Z., Wang, Y., and Zhang, Z. (2019). Linking rheology and printability of a multicomponent gel system of carrageenan-xanthan-starch in extrusion based additive manufacturing. Minerva Endocrinol. 44, 413–415. https://doi. org/10.1016/j.foodhyd.2018.08.026.
- Wei, P., Cipriani, C.E., and Pentzer, E.B. (2021). Thermal energy regulation with 3D printed polymer-phase change material composites. Matter 4, 1975–1989. https://doi.org/10.1016/j. matt.2021.03.019.
- Saadi, M.A.S.R., Maguire, A., Pottackal, N.T., Thakur, M.S.H., Ikram, M.M., Hart, A.J., Ajayan, P.M., and Rahman, M.M. (2022). Direct ink writing: a 3D printing technology for diverse materials. Adv. Mater. 34, 2108855. https://doi. org/10.1002/adma.202108855.
- Zhu, C., Han, T.Y.-J., Duoss, E.B., Golobic, A.M., Kuntz, J.D., Spadaccini, C.M., and Worsley, M.A. (2015). Highly compressible 3D periodic graphene aerogel microlattices. Nat. Commun. 6, 6962. https://doi.org/10.1038/ ncomms/7962.
- Sommer, M.R., Alison, L., Minas, C., Tervoort, E., Rühs, P.A., and Studart, A.R. (2017). 3D printing of concentrated emulsions into multiphase biocompatible soft materials. Soft Matter 13, 1794–1803. https://doi.org/10.1039/ C6SM02682F.
- Alison, L., Menasce, S., Bouville, F., Tervoort, E., Mattich, I., Ofner, A., and Studart, A.R. (2019). 3D printing of sacrificial templates into hierarchical porous materials. Sci. Rep. 9, 409. https://doi.org/10.1038/s41598-018-36789-z.
- Hu, Y., Wang, J., Li, X., Hu, X., Zhou, W., Dong, X., Wang, C., Yang, Z., and Binks, B.P. (2019). Facile preparation of bioactive nanoparticle/ poly (e-caprolactone) hierarchical porous scaffolds via 3D printing of high internal phase Pickering emulsions. J. Colloid Interface Sci. 545, 104–115. https://doi.org/10.1016/j.jcis. 2019.03.024.

- Sears, N.A., Dhavalikar, P.S., and Cosgriff-Hernandez, E.M. (2016). Emulsion inks for 3D printing of high porosity materials. Macromol. Rapid Commun. 37, 1369–1374. https://doi. org/10.1002/marc.201600236.
- Chan, S.S.L., Sesso, M.L., and Franks, G.V. (2020). Direct ink writing of hierarchical porous alumina-stabilized emulsions: Rheology and printability. J. Am. Ceram. Soc. 103, 5554–5566. https://doi.org/10.1111/jace.17305.
- Minas, C., Carnelli, D., Tervoort, E., and Studart, A.R. (2016). 3D printing of emulsions and foams into hierarchical porous ceramics. Adv. Mater. 28, 9993–9999. https://doi.org/10. 1002/adma.201603390.
- Liu, Q., and Zhai, W. (2022). Hierarchical porous ceramics with distinctive microstructures by emulsion-based direct ink writing. ACS Appl. Mater. Interfaces 14, 32196–32205. https://doi. org/10.1021/acsami.2c03245.
- 35. Menner, A., and Bismarck, A. (2006). New evidence for the mechanism of the pore formation in polymerising high internal phase emulsions or why polyHIPEs have an interconnected pore network structure. In 1 (Wiley Online Library)), pp. 19–24.
- McDevitt, K.M., Thorson, T.J., Botvinick, E.L., Mumm, D.R., and Mohraz, A. (2019). Microstructural characteristics of bijeltemplated porous materials. Materialia 7, 100393. https://doi.org/10.1016/j.mtla.2019. 100393.
- Debnath, D., Zhao, X., Anas, M., Kulhanek, D.L., Oh, J.H., and Green, M.J. (2020). Radio frequency heating and reduction of graphene oxide and graphene oxide-polyvinyl alcohol composites. Carbon 169, 475–481. https://doi. org/10.1016/j.carbon.2020.07.076.
- Habib, T., Patil, N., Zhao, X., Prehn, E., Anas, M., Lutkenhaus, J.L., Radovic, M., and Green, M.J. (2019). Heating of Ti3C2Tx MXene/ polymer composites in response to Radio Frequency fields. Sci. Rep. 9, 16489. https://doi. org/10.1038/s41598-019-52972-2.
- Sweeney, C.B., Moran, A.G., Gruener, J.T., Strasser, A.M., Pospisil, M.J., Saed, M.A., and Green, M.J. (2018). Radio frequency heating of carbon nanotube composite materials. ACS Appl. Mater. Interfaces 10, 27252–27259. https://doi.org/10.1021/acsami.8b06268.
- Akbari, A., Cunning, B.V., Joshi, S.R., Wang, C., Camacho-Mojica, D.C., Chatterjee, S., Modepalli, V., Cahoon, C., Bielawski, C.W., Bakharev, P., et al. (2020). Highly ordered and dense thermally conductive graphitic films from a graphene oxide/reduced graphene oxide mixture. Matter 2, 1198–1206. https:// doi.org/10.1016/j.matt.2020.02.014.
- Thickett, S.C., and Zetterlund, P.B. (2015). Graphene oxide (GO) nanosheets as oil-in-water emulsion stabilizers: Influence of oil phase polarity. J. Colloid Interface Sci. 442, 67–74. https://doi.org/10.1016/j.jcis.2014. 11.047
- Kim, J., Cote, L.J., Kim, F., Yuan, W., Shull, K.R., and Huang, J. (2010). Graphene oxide sheets at interfaces. J. Am. Chem. Soc. 132, 8180–8186. https://doi.org/10.1021/ja102777p.
- 43. Kim, F., Cote, L.J., and Huang, J. (2010). Graphene oxide: surface activity and



- two-dimensional assembly. Adv. Mater. 22, 1954–1958. https://doi.org/10.1002/adma. 200903932.
- Luo, Q., Wei, P., and Pentzer, E. (2016). Hollow microcapsules by stitching together of graphene oxide nanosheets with a difunctional small molecule. Carbon 106, 125–131. https://doi.org/10.1016/j.carbon. 2016.05.024.
- Luo, Q., Wang, Y., Yoo, E., Wei, P., and Pentzer, E. (2018). Ionic liquid-containing pickering emulsions stabilized by graphene oxide-based surfactants. Langmuir 34, 10114–10122. https:// doi.org/10.1021/acs.langmuir.8b02011.
- Wang, Y., Wei, P., Zhou, Q., Cipriani, C., Qi, M., Sukhishvili, S., and Pentzer, E. (2022). Temperature-Dependent Capsule Shell Bonding and Destruction Based on Hindered Poly (urea-urethane) Chemistry. Chem. Mater. 34, 5821–5831. https://doi.org/10.1021/acs. chemmater.2c00415.
- Barnes, H.A. (1994). Rheology of emulsions—a review. Colloids Surf. A Physicochem. Eng. Asp. 91, 89–95. https://doi.org/10.1016/0927-7757(93)02719-U.
- Cai, D., Clegg, P.S., Li, T., Rumble, K.A., and Tavacoli, J.W. (2017). Bijels formed by direct mixing. Soft Matter 13, 4824–4829. https://doi. org/10.1039/c7sm00897j.
- Hao, B., and Yu, W. (2019). A new solid-like state for liquid/liquid/particle mixtures with bicontinuous morphology of concentrated emulsion and concentrated suspension. Langmuir 35, 9529–9537. https://doi.org/10. 1021/acs.langmuir.9b01088.
- 50. Qiu, R., Wang, K., Tian, H., Liu, X., Liu, G., Hu, Z., and Zhao, L. (2022). Analysis on the printability and rheological characteristics of

- bigel inks: Potential in 3D food printing. Food Hydrocolloids 129, 107675. https://doi.org/10.1016/j.foodhyd.2022.107675.
- Wei, P., Cipriani, C., Hsieh, C.-M., Kamani, K., Rogers, S., and Pentzer, E. (2023). Go with the flow: Rheological requirements for direct ink write printability. J. Appl. Phys. 134. https://doi. org/10.1063/5.0155896.
- Zhu, Z., Chen, H., Chen, Q., Liu, C., Noh, K., Yao, H., Kotaki, M., and Sue, H.-J. (2022). Fracture behavior of hybrid epoxy nanocomposites based on multi-walled carbon nanotube and core-shell rubber. Nano Materials Science 4, 251-258. https://doi.org/ 10.1016/j.nanoms.2021.07.006.
- Zhu, Z., Baker, J., Liu, C., Zhao, M., Kotaki, M., and Sue, H.-J. (2021). High performance epoxy nanocomposites based on dual epoxide modified α-Zirconium phosphate nanoplatelets. Polymer 212, 123154. https:// doi.org/10.1016/j.polymer.2020.123154.
- Vashisth, A., Upama, S.T., Anas, M., Oh, J.-H., Patil, N., and Green, M.J. (2021). Radio frequency heating and material processing using carbon susceptors. Nanoscale Adv. 3, 5255–5264. https://doi.org/10.1039/ D1NA00217A.
- Sarmah, A., Desai, S.K., Crowley, A.G., Zolton, G.C., Tezel, G.B., Harkin, E.M., Tran, T.Q., Arole, K., and Green, M.J. (2022). Additive manufacturing of nanotube-loaded thermosets via direct ink writing and radio-frequency heating and curing. Carbon 200, 307–316. https://doi.org/10.1016/j.carbon.2022.08.063.
- Anas, M., Zhao, Y., Saed, M.A., Ziegler, K.J., and Green, M.J. (2019). Radio frequency heating of metallic and semiconducting single-

- walled carbon nanotubes. Nanoscale 11, 9617–9625. https://doi.org/10.1039/C9NR01600G.
- 57. Cao, H., Wang, Y., Sarmah, A., Liu, K.-W., Tan, Z., Arole, K.D., Lutkenhaus, J.L., Radovic, M., Green, M.J., and Pentzer, E.B. (2022). Electrically conductive porous Ti3C2T x MXene-polymer composites from high internal phase emulsions (HIPEs). 2D Mater. 9, 044004. https://doi.org/10.1088/2053-1583/ac914c.
- Cao, H., Escamilla, M., Arole, K.D., Holta, D., Lutkenhaus, J.L., Radovic, M., Green, M.J., and Pentzer, E.B. (2021). Flocculation of MXenes and their use as 2D particle surfactants for capsule formation. Langmuir 37, 2649–2657. https://doi.org/10.1021/acs.langmuir.0c03244.
- Zhao, X., Vashisth, A., Prehn, E., Sun, W., Shah, S.A., Habib, T., Chen, Y., Tan, Z., Lutkenhaus, J.L., Radovic, M., and Green, M.J. (2019). Antioxidants unlock shelf-stable Ti3C2Tx (MXene) nanosheet dispersions. Matter 1, 513–526. https://doi.org/10.1016/j.matt.2019. 05.020.
- Gao, H., Benitez, R., Son, W., Arroyave, R., and Radovic, M. (2016). Structural, physical and mechanical properties of Ti3 (Al1 – xSix) C2 solid solution with x= 0–1. Mater. Sci. Eng., A 676, 197–208. https://doi.org/10.1016/j.msea. 2016.08.098.
- Dimiev, A., Kosynkin, D.V., Alemany, L.B., Chaguine, P., and Tour, J.M. (2012). Pristine graphite oxide. J. Am. Chem. Soc. 134, 2815– 2822. https://doi.org/10.1021/ja211531y.
- 62. Hu, L., Benitez, R., Basu, S., Karaman, I., and Radovic, M. (2012). Processing and characterization of porous Ti2AlC with controlled porosity and pore size. Acta Mater. 60, 6266–6277. https://doi.org/10.1016/j.actamat.2012.07.052.

Matter, Volume 6

# **Supplemental information**

Morphology map-guided identification of bijel ink for producing conductive porous structures

Yifei Wang, Ciera Cipriani, Chia-Min Hsieh, Huaixuan Cao, Anubhav Sarmah, Kai-Wei Liu, Zeyi Tan, Micah J. Green, Miladin Radovic, Peiran Wei, and Emily B. Pentzer

**Table S1.** Sample compositions of each ink. Top-to-bottom columns have same GO/water concentration, increasing GO wt%, and decreasing resin/water ratio; left-to-right in a row show increasing GO/water concentration, increasing GO wt%, and similar resin/water ratio. Water-in-resin emulsion (W/R[E]) (red); combination of water-in-resin emulsion and bijel (W/R[E]+[B], blue); bijel ([B], yellow); resin-in-water condensed emulsion (R/W[CE], green); resin-in-water emulsion (R/W[E], magenta).

	20 mg/mL				40	mg/mL		60 mg/mL			80 mg/mL			100 mg/mL					
#	GO (mg)	Water (mg)	Resin (mg)	#	GO (mg)	Water (mg)	Resin (mg)	#	GO (mg)	Water (mg)	Resin (mg)	#	GO (mg)	Water (mg)	Resin (mg)	#	GO (mg)	Water (mg)	Resin (mg)
1	2	100	898	9	4	100	896	17	6	100	894	25	8	100	892	33	10	100	890
2	4	200	<b>796</b>	10	8	200	<b>792</b>	18	12	200	788	26	16	200	784	34	20	200	780
3	6	300	694	11	12	300	688	19	18	300	682	27	24	300	676	35	30	300	670
4	8	400	<b>592</b>	12	16	400	584	20	24	400	<b>576</b>	28	32	400	568	36	40	400	560
5	10	500	490	13	20	500	480	21	30	500	470	29	40	500	460	37	50	500	450
6	12	600	388	14	24	600	376	22	36	600	364	30	48	600	352	38	60	600	340
7	14	700	286	15	28	700	272	23	42	700	258	31	56	700	244	39	70	700	230
8	16	800	184	16	32	800	168	24	48	800	152	32	64	800	136	40	80	800	120

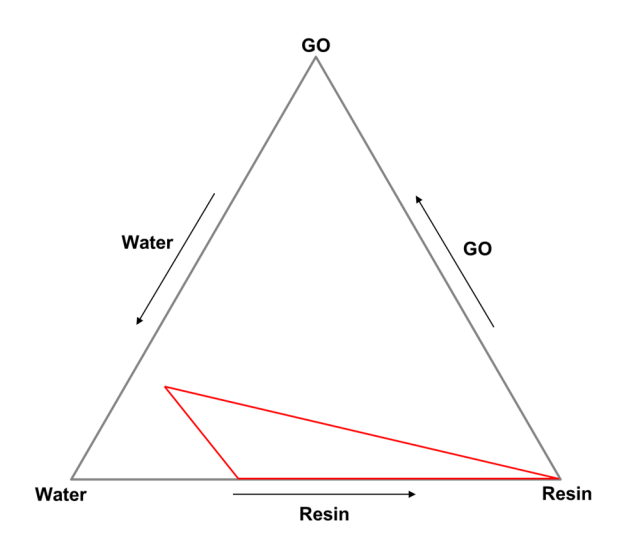


**Figure S1.** Samples selected for constructing the morphology map are within the red obtuse triangle area.

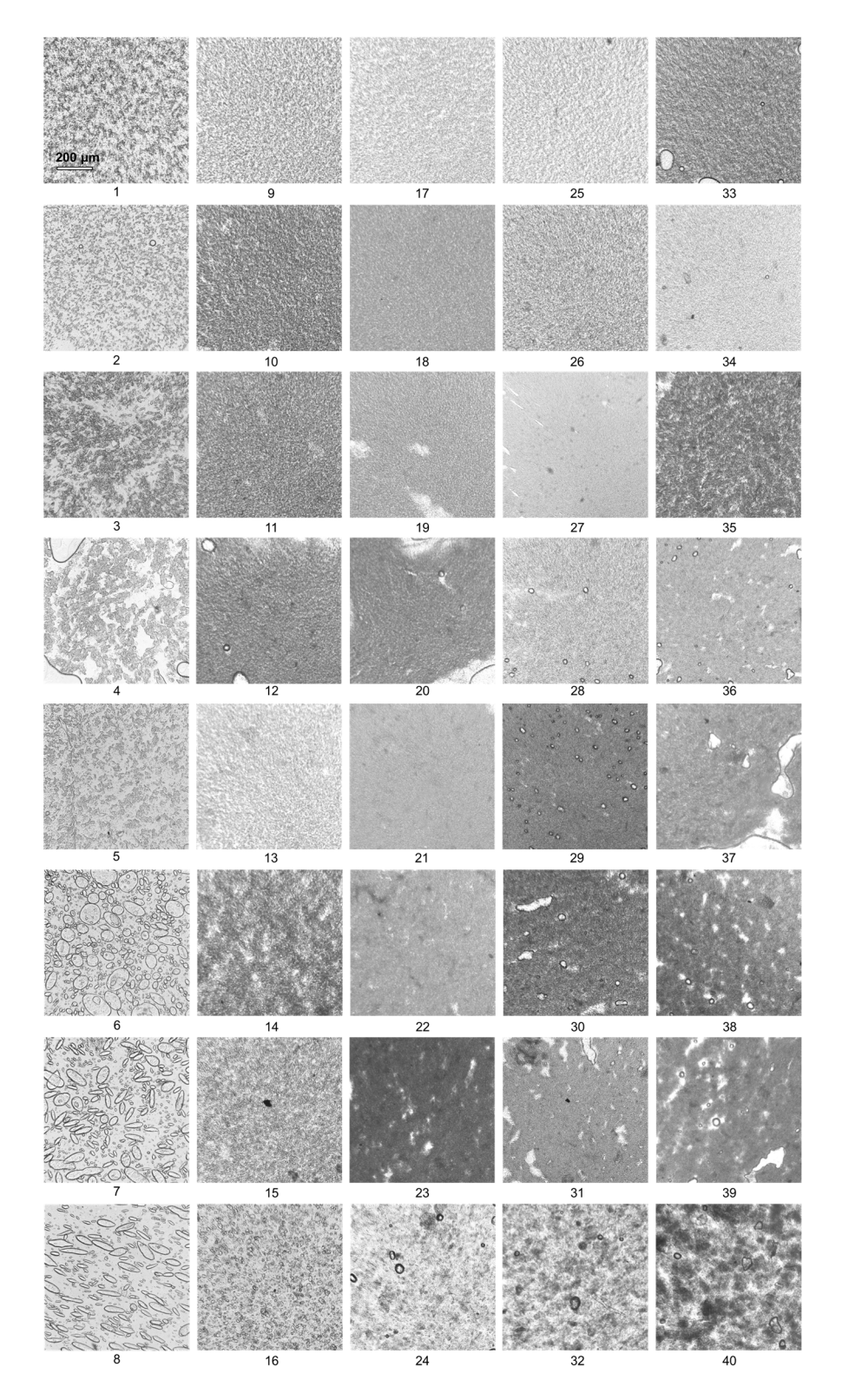


**Figure S2.** Optical microscope images of different samples. Top-to-bottom columns have the same GO/water concentration, increasing GO wt%, and decreasing resin/water ratio; left-to-right in a row show increasing GO/water concentration, increasing GO wt%, and similar resin/water ratio.

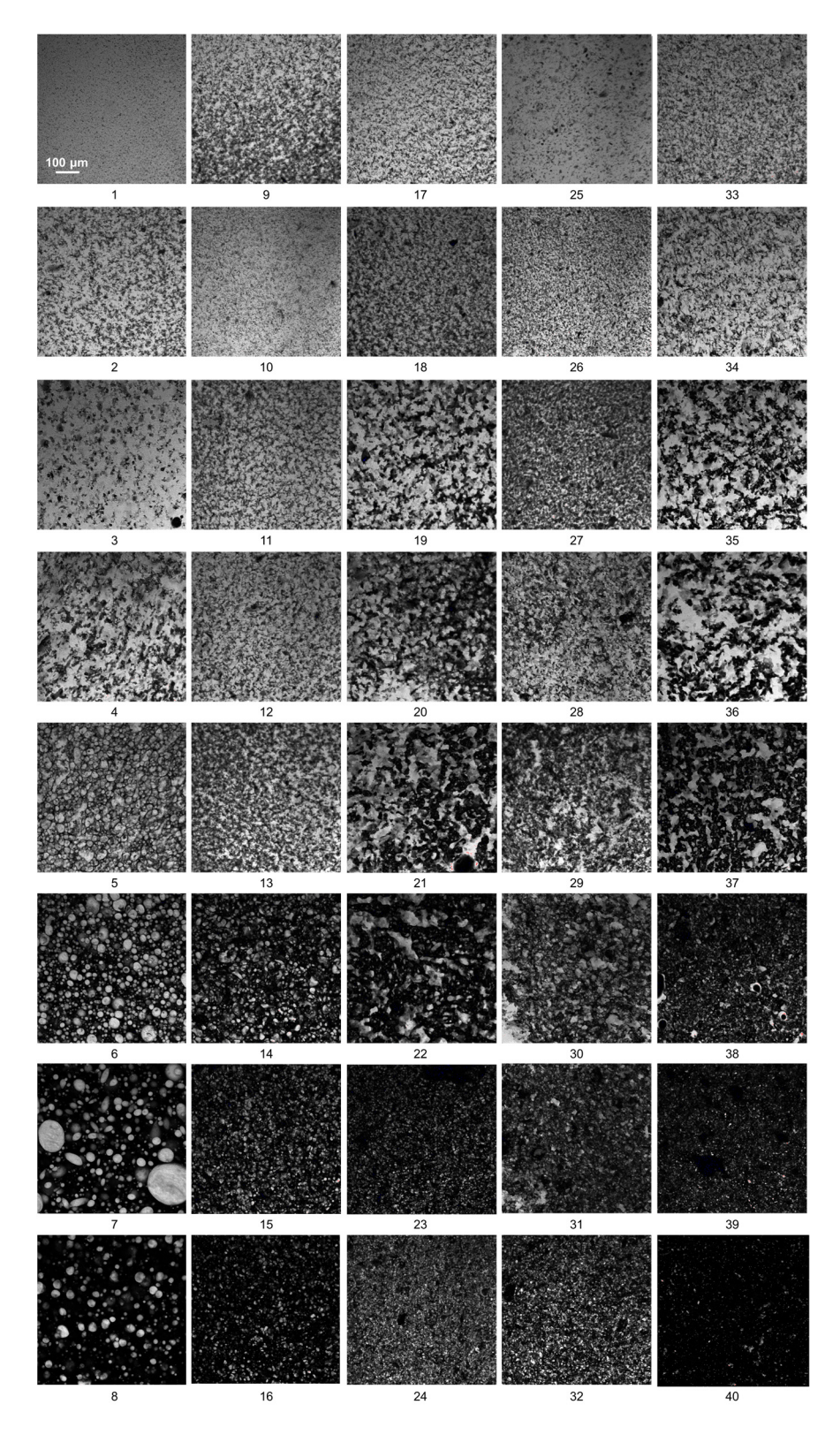


**Figure S3.** Fluorescence confocal microscope images of different samples. Top-to-bottom columns have the same GO/water concentration, increasing GO wt%, and decreasing resin/water ratio; left-to-right in a row show increasing GO/water concentration, increasing GO wt%, and similar resin/water ratio.

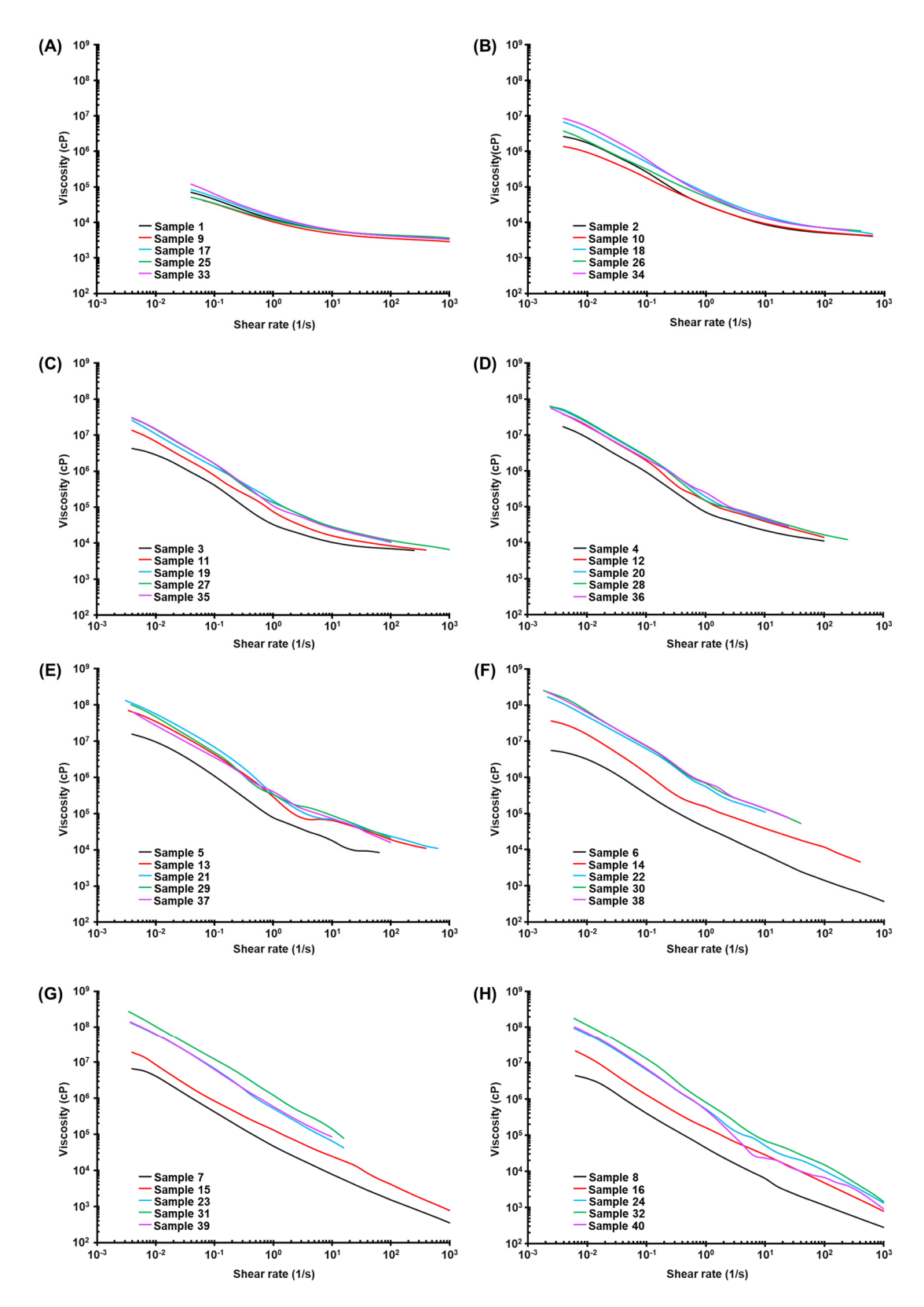


**Figure S4.** Viscosity as a function of shear rate. Samples on each graph have a similar resin/water mass ratio and increasing GO wt% as sample number increases (graphs A-H correspond to sample points on **Figure 2**, line A-H).

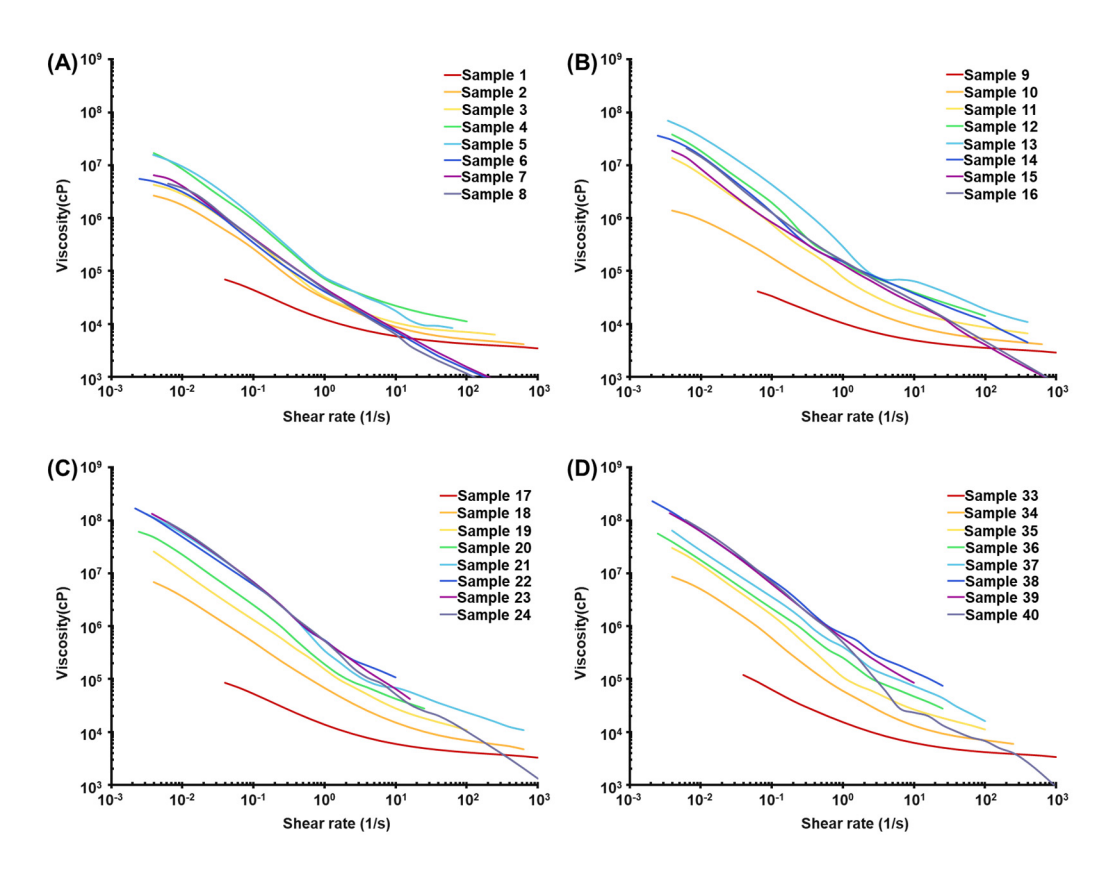


**Figure S5.** Viscosity as a function of shear rate. Samples on each graph have decreasing resin/water mass ratio and increasing GO wt% as sample number increases (graphs A-D correspond to sample points on **Figure 2**, line u, v, w, y).

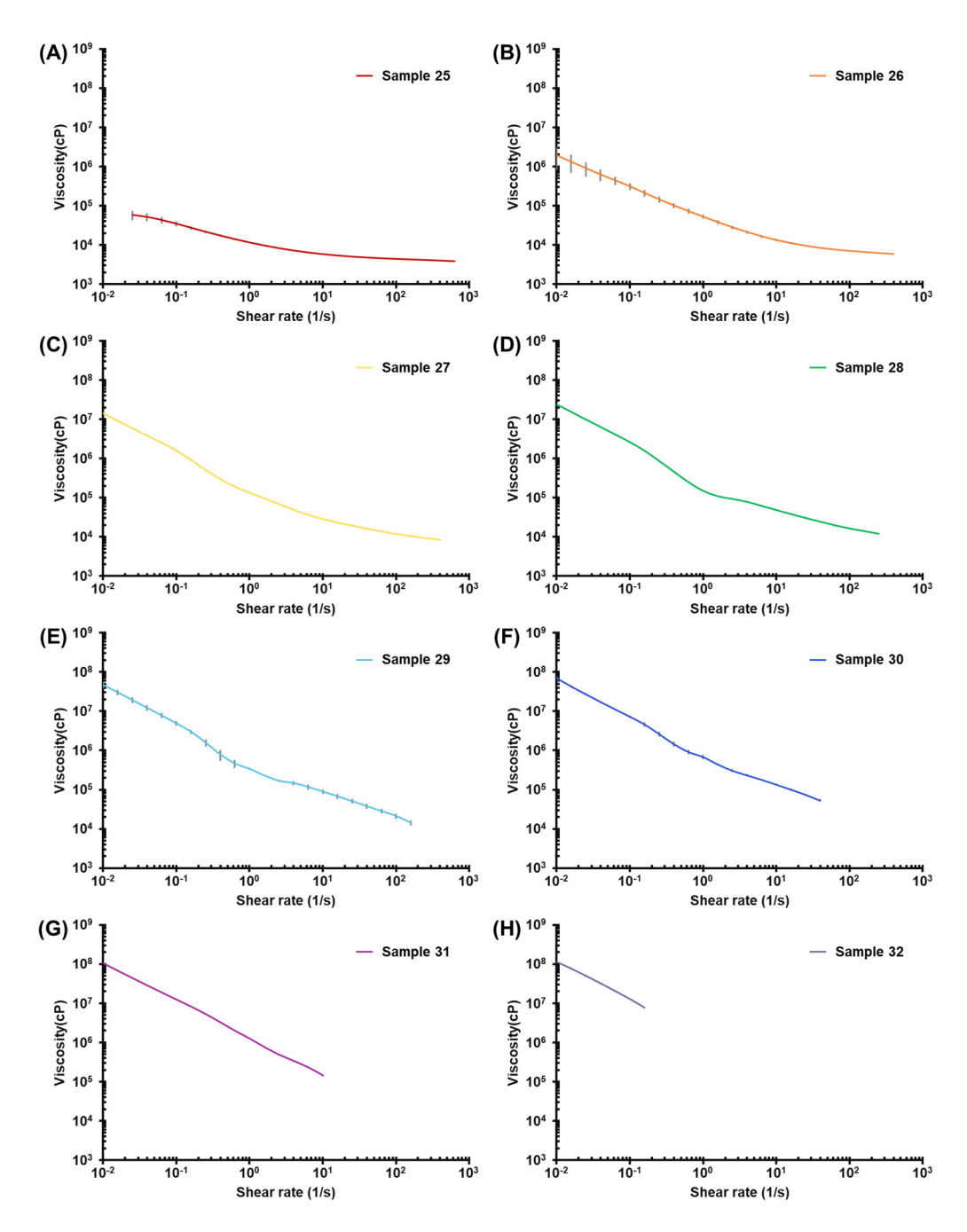


**Figure S6.** Viscosity as a function of shear rate for samples in **Figure 3A** (graphs A-H correspond to sample points on **Figure 2**, line x). Error bars indicate standard deviation (n=3).

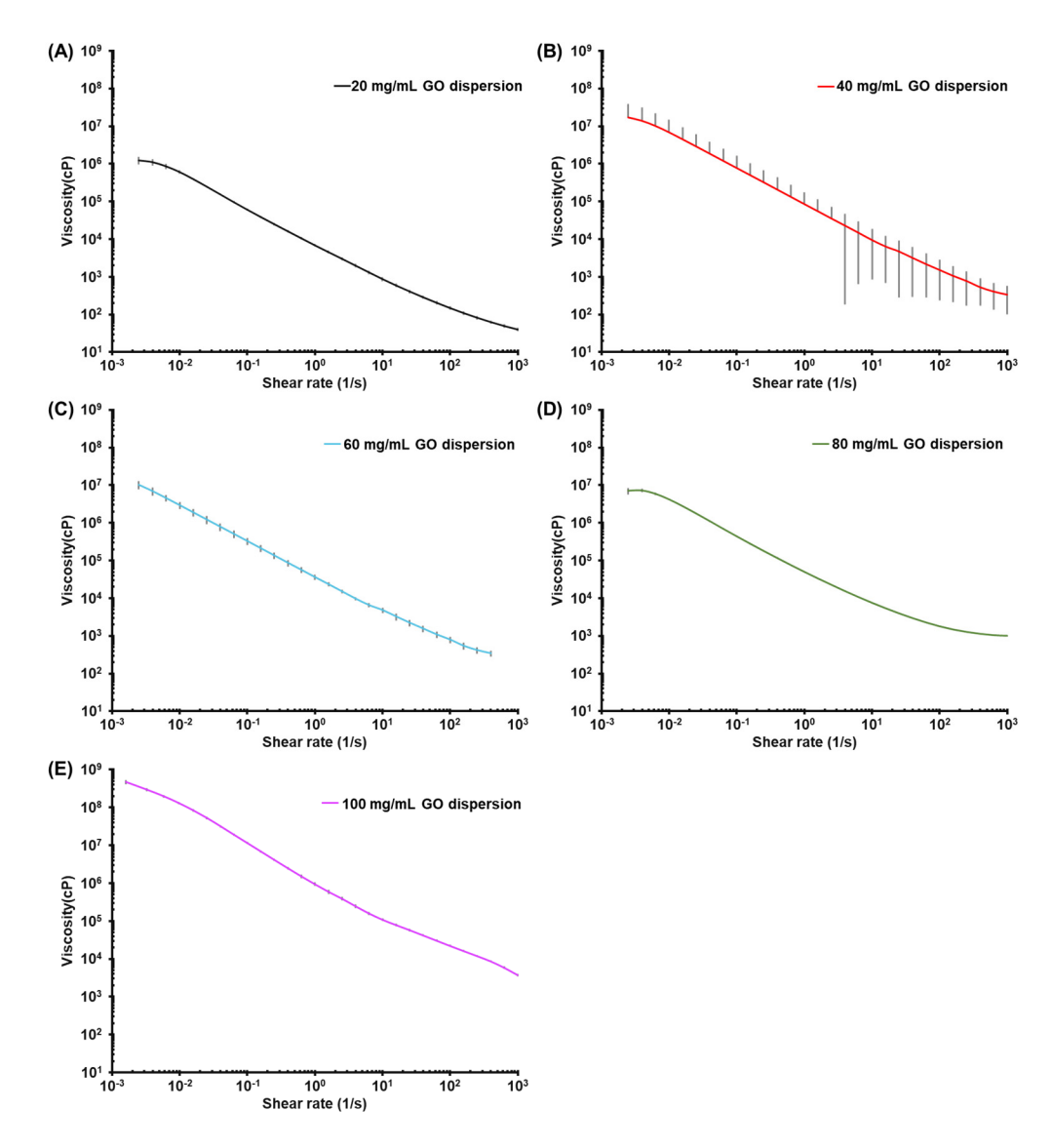


**Figure S7.** Viscosity as a function of shear rate for different GO dispersion concentrations (graphs A-E correspond to 20 mg/mL-100 mg/mL GO/water concentration, respectively). Error bars indicate standard deviation (n=3).

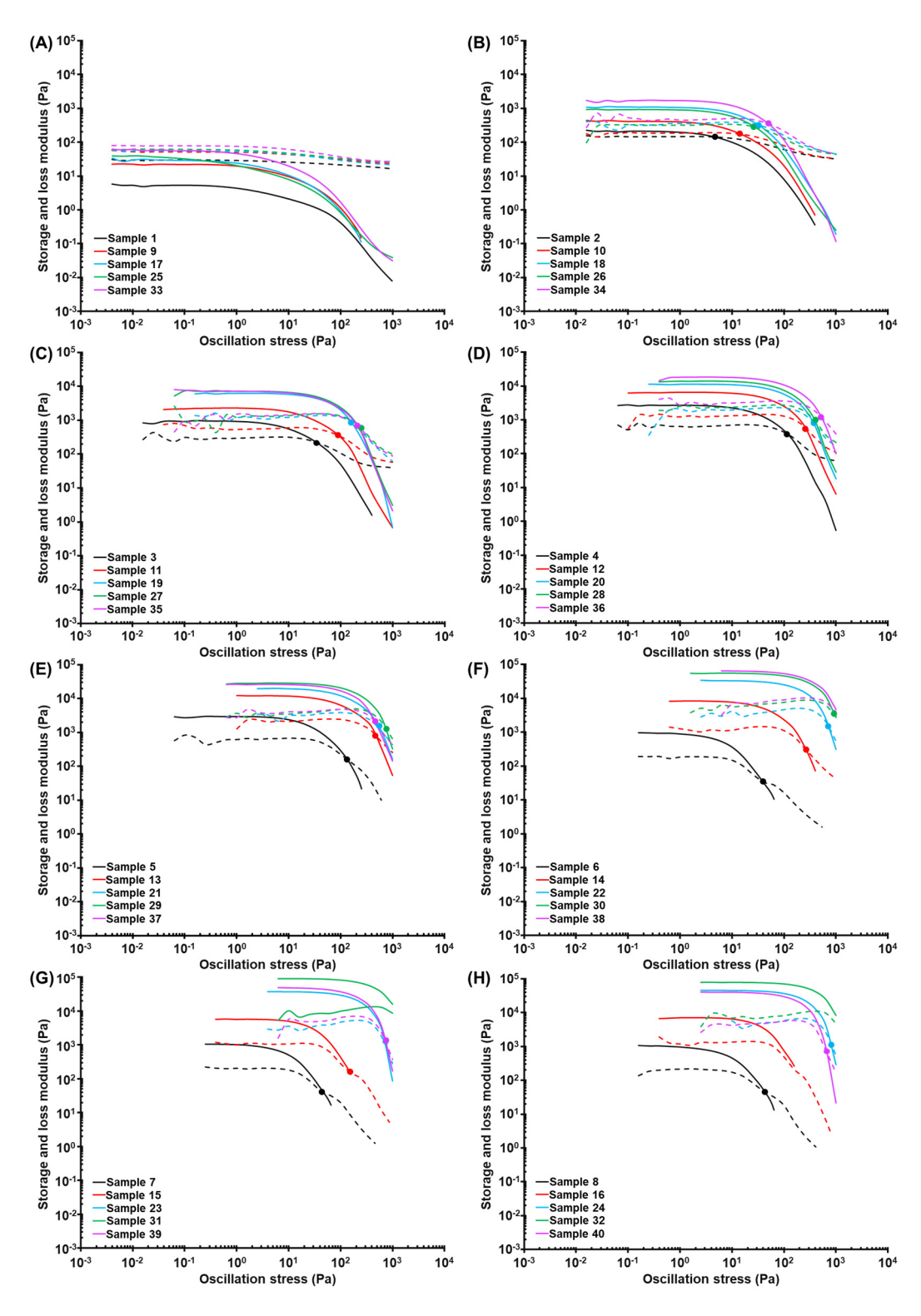


**Figure S8.** Storage modulus (solid line) and loss modulus (dashed line) as a function of oscillation stress. Samples in each graph have a similar resin/water mass ratio and increasing GO wt% as sample number increases (graphs A-H correspond to sample points on **Figure 2**, line A-H).

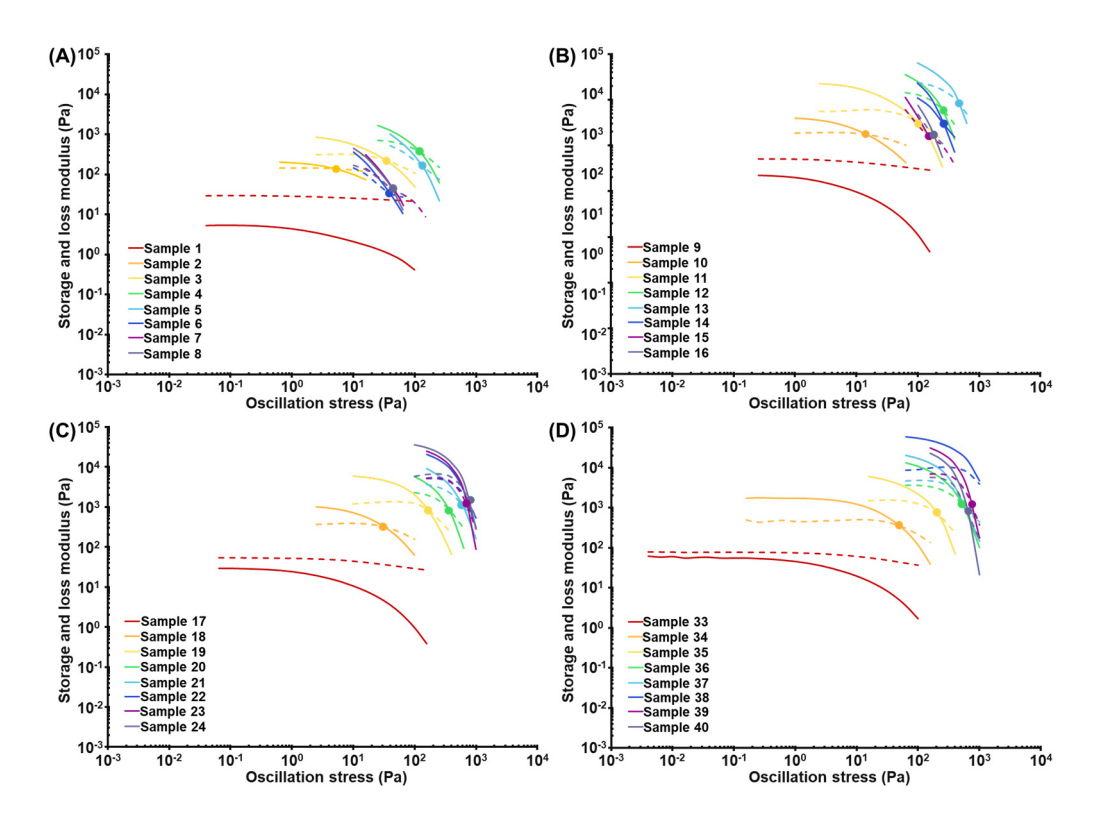


**Figure S9.** Storage modulus (solid line) and loss modulus (dashed line) as a function of oscillation stress. Samples in each graph have decreasing resin/water mass ratio and increasing GO wt% as sample number increases (graphs A-D correspond to sample points on **Figure 2**, line u, v, w, y).

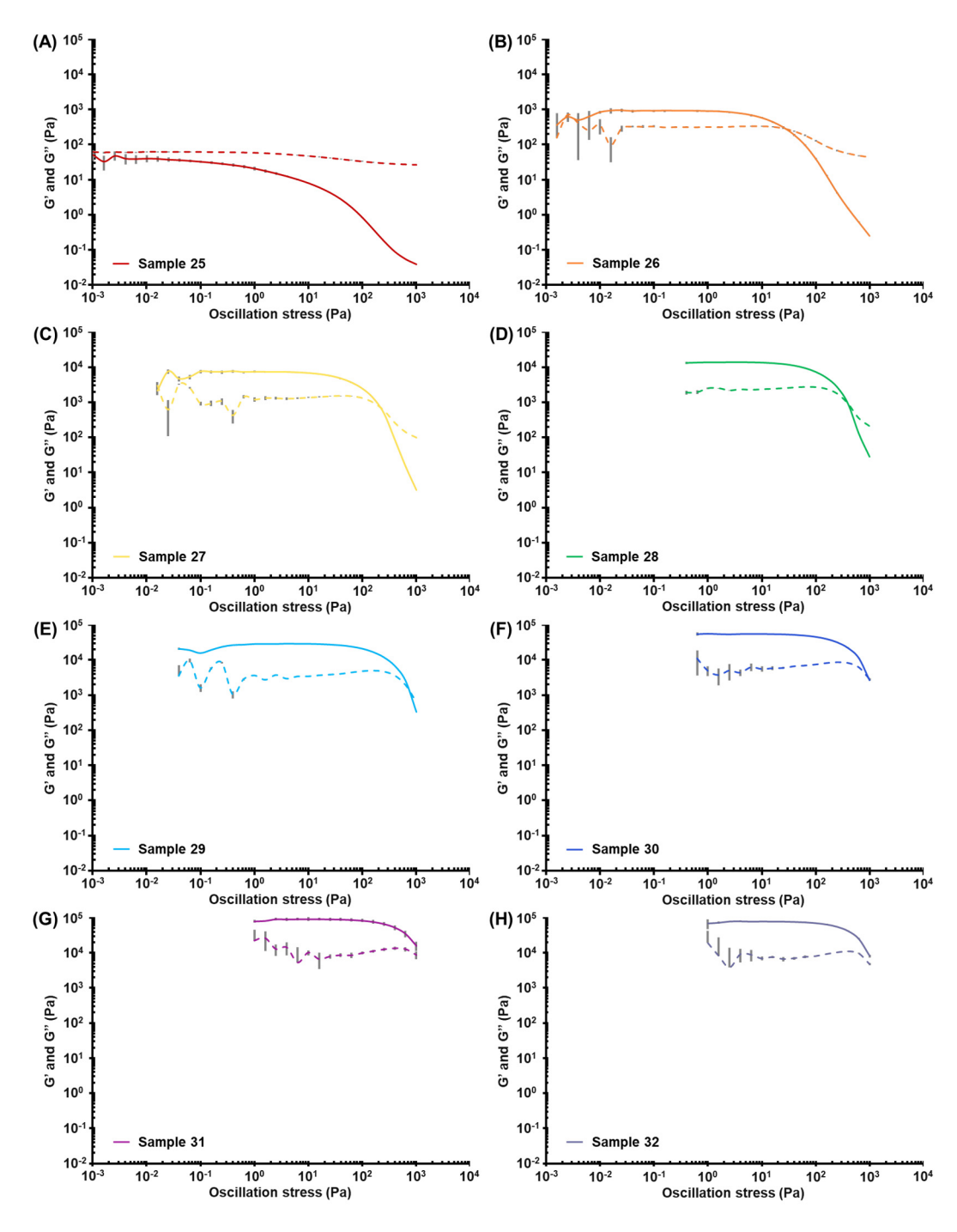


**Figure S10.** Storage modulus and loss modulus as a function of oscillation stress for samples in **Figure 3B** (graphs A-H correspond to sample points on **Figure 2**, line x). Error bars indicate standard deviation (n=3).

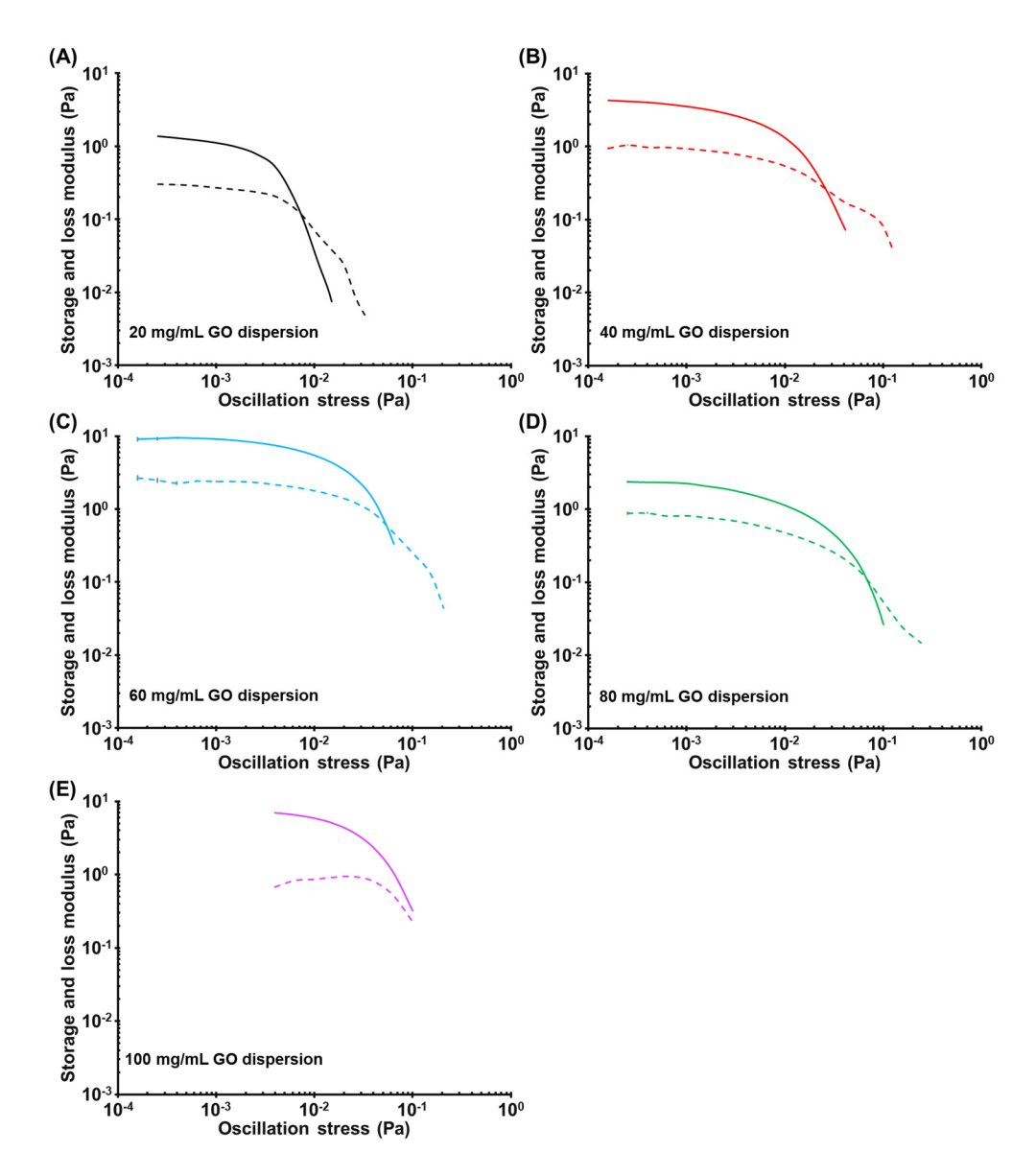


**Figure S11.** Storage modulus (solid line) and loss modulus (dashed line) as a function of oscillation stress for different GO dispersion concentrations (graphs A-E correspond to 20 mg/mL-100 mg/mL GO/water concentration, respectively). Error bars indicate standard deviation (n=3).

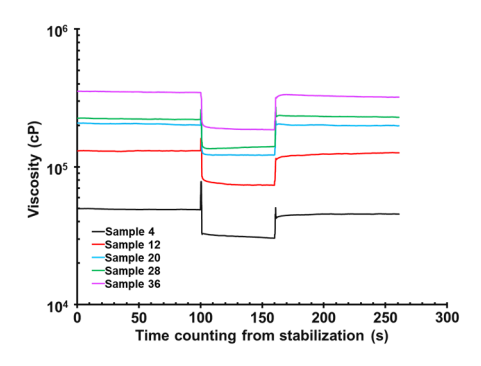


**Figure S12.** Representative three-interval thixotropy tests of samples 4, 12, 20, 28, 36 (corresponding to sample points on **Figure 2**, line D).

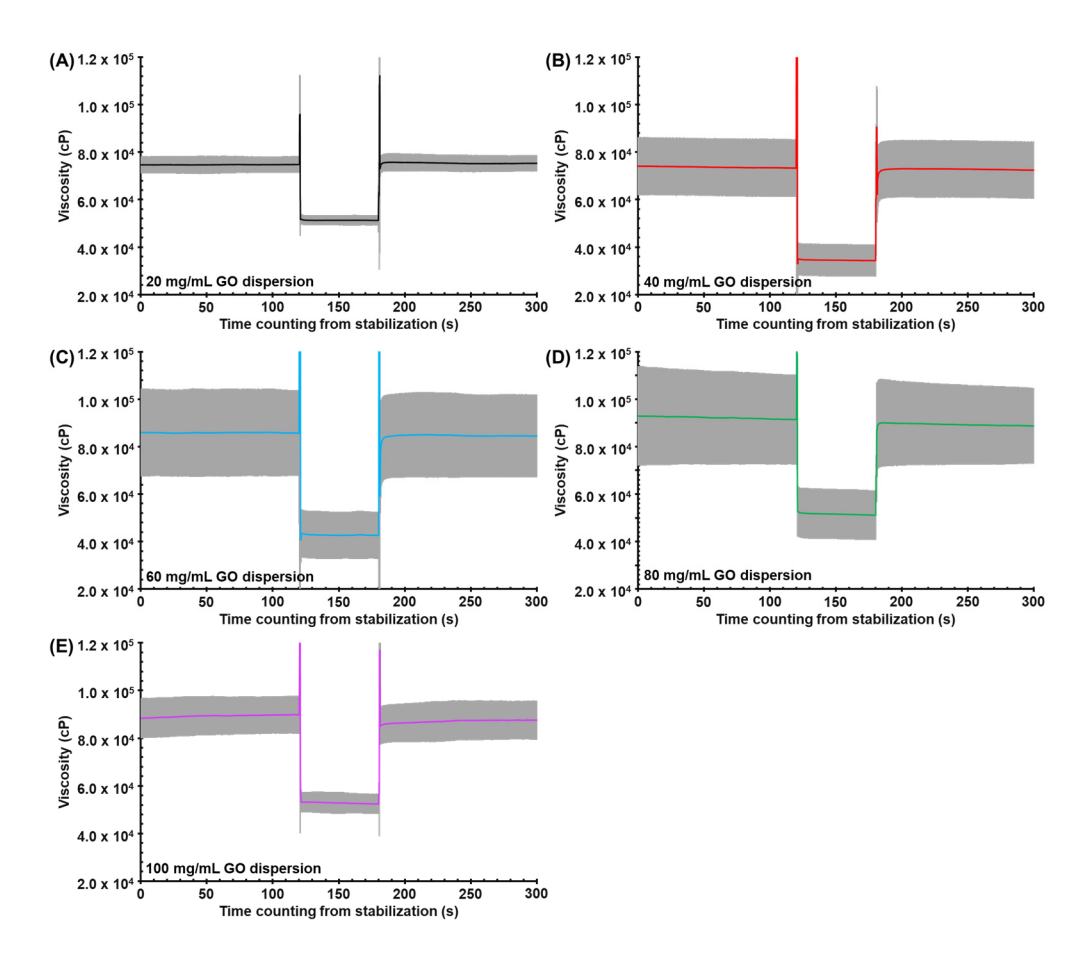


**Figure S13.** Thixotropic test of GO dispersions (graphs A-E correspond to 20 mg/mL-100 mg/mL GO/water concentration, respectively; gray area represents standard deviation, n=3).

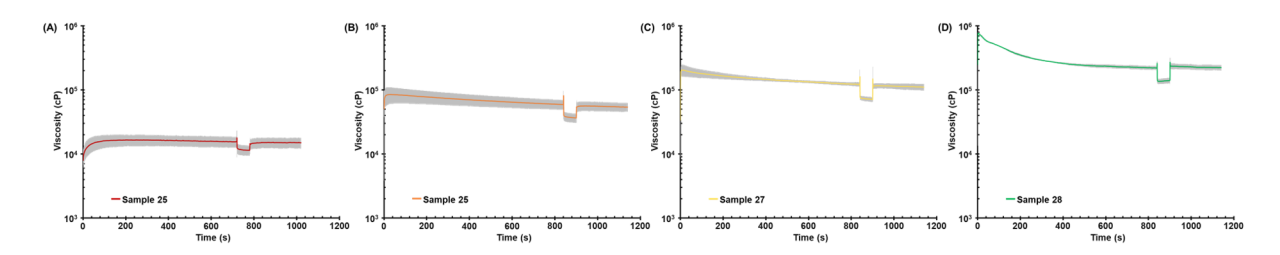


**Figure S14.** Viscosity over time during the three-interval thixotropy tests for samples in **Figure 3C** with gray area representing standard deviation (n=3) (graphs A-D correspond to sample points on **Figure 2**, line x).

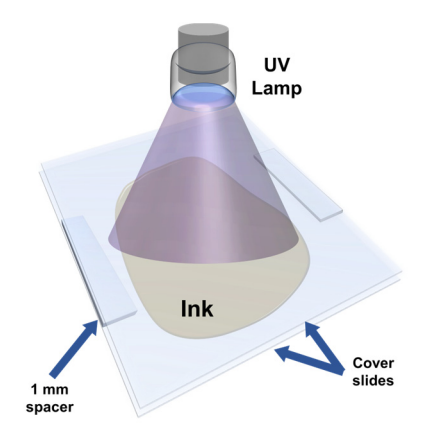
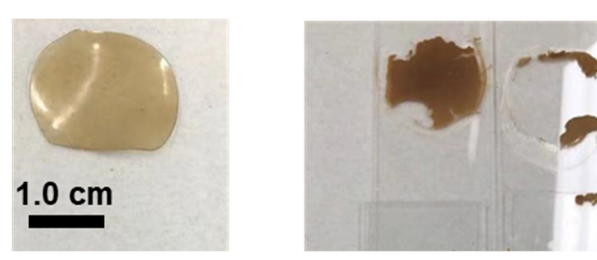


Figure S15. Schematic illustration of curability test.



**Figure S16.** Representative images of samples after irradiation with UV light. Left: successful curing identified by removal of foam from the glass slide; right: unable to form intact foam after curing.

Table S2. Table summarizing composition and conductivity of obtained porous structures.

20mg/mL GO/Water Dispersion										
Sample identity	Resin (mg)	GO (mg)	Water	GO wt% of obtained porous structure	Conductivity of obtained porous structure (mS/cm)					
1	898	2	100	0.22	N/A					
2	796	4	200	0.50	N/A					
3	694	6		0.86	N/A					
4	592	8	400	1.3	N/A					
5	490	10	500	N/A	N/A					
6	388	12	600	N/A	N/A					
7	286	14	700	N/A	N/A					
8	184	16	800	N/A	N/A					

	40mg/mL GO/Water Dispersion											
Sample identity	Resin (mg)	GO (mg)	Water (mg)	GO wt% of obtained porous structure	Conductivity of obtained porous structure (mS/cm)							
9	896	4	100	0.44	N/A							
10	792	8	200	1.0	N/A							
11	688	12	300	1.7	0.0970							
12	584	16	400	2.7	0.350							
13	480	20	500	N/A	N/A							
14	376	24	600	N/A	N/A							
15	272	28	700	N/A	N/A							
16	168	32	800	N/A	N/A							

60mg/mL GO/Water Dispersion							
	Sample identity	Resin (mg)	GO (mg)	Water (mg)	GO wt% of obtained porous structure	Conductivity of obtained porous structure (mS/cm)	
	17	894	6	100	0.67	N/A	
	18	788	12	200	1.5	0.0970	
	19	682	18	300	2.6	0.462	
	20	576	24	400	4.0	1.27	
	21	470	30	500	N/A	N/A	
	22	364	36	600	N/A	N/A	
	23	258	42	700	N/A	N/A	
	24	152	48	800	N/A	N/A	

Sample identity Resin (mg) GO (mg) Water (mg) of obtained porous structure										
Sample identity         Resin (mg)         GO (mg)         Water (mg)         of obtained porous structure         of obtained porous structure           25         892         8         100         0.89         N/A           26         784         16         200         2.0         0.30           27         676         24         300         3.4         1.23           28         568         32         400         5.3         1.29           29         460         40         500         N/A         N/A           30         352         48         600         N/A         N/A           21         244         56         700         N/A         N/A										
26         784         16         200         2.0         0.30           27         676         24         300         3.4         1.23           28         568         32         400         5.3         1.29           29         460         40         500         N/A         N/A           30         352         48         600         N/A         N/A           21         244         56         700         N/A         N/A			GO (mg)		of obtained porous	Conductivity of obtained porous structure (mS/cm)				
27         676         24         300         3.4         1.23           28         568         32         400         5.3         1.29           29         460         40         500         N/A         N/A           30         352         48         600         N/A         N/A           21         244         56         700         N/A         N/A	25	892	8	100	0.89	N/A				
28         568         32         400         5.3         1.29           29         460         40         500         N/A         N/A           30         352         48         600         N/A         N/A           21         244         56         700         N/A         N/A	26	784	16	200	2.0	0.30				
29         460         40         500         N/A         N/A           30         352         48         600         N/A         N/A           21         244         56         700         N/A         N/A	27	676	24	300	3.4	1.23				
30 352 48 600 N/A N/A 21 244 56 700 N/A N/A	28	568	32	400	5.3	1.29				
21 244 56 700 N/A N/A	29	460	40	500	N/A	N/A				
	30	352	48	600	N/A	N/A				
32 136 64 800 N/A N/A	21	244	56	700	N/A	N/A				
	32	136	64	800	N/A	N/A				

	100mg/mL GO/Water Dispersion											
Sample identity			Water (mg)	GO wt% of obtained porous structure	Conductivity of obtained porous structure (mS/cm)							
33	890	10	100	1.1	0.236							
34	780	20	200	2.5	0.781							
35	670	30	300	4.3	1.31							
36	560	40	400	6.7	2.15							
37	450	50	500	N/A	N/A							
38	340	60	600	N/A	N/A							
39	230	70	700	N/A	N/A							
40	120	80	800	N/A	N/A							

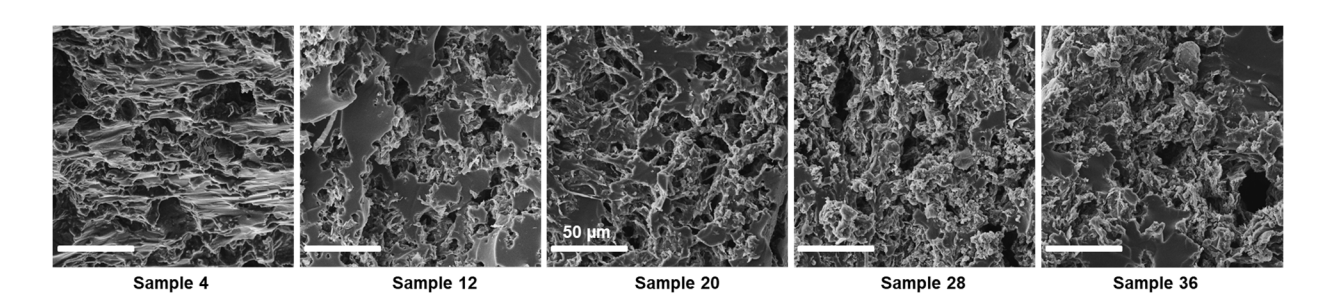


**Figure S17.** SEM images of cured samples with similar resin/water ratios but increasing GO wt% (samples 4, 12, 20, 28, and 36).

**Table S3.** Table summarizing bulk density and calculated porosity of selected obtained porous structures.

Sample identity		GO (mg)	Water (mg)	GO wt% of obtained porous structure	Conductivity of obtained porous structure (mS/cm)	Bulk density (g/cm³)	Calculated porosity (%)	Theoretical porosity (%)
4	592	8	400	1.3	N/A	1.01 ± 0.03	10.4 ± 0.03	15.2 ± 0.02
12	584	16	400	2.7	0.350	0.91 ± 0.05	19.3 ± 0.07	22.2 ± 0.05
19	682	18	300	2.6	0.462	$0.82 \pm 0.02$	27.2 ± 0.02	23.9 ± 0.05
20	576	24	400	4.0	1.27	0.77 ± 0.03	31.5 ± 0.03	34.7± 0.03
25	892	8	100	0.89	N/A	1.11 ± 0.05	1.59 ± 0.05	6.30 ± 0.03
26	784	16	200	2.0	0.30	1.02 ± 0.02	9.57 ± 0.05	12.8 ± 0.05
27	676	24	300	3.4	1.23	$0.82 \pm 0.03$	27.3 ± 0.02	27.5 ± 0.06
28	568	32	400	5.3	1.29	0.72 ± 0.03	35.8 ± 0.04	36.1 ± 0.03
36	560	40	400	6.7	2.15	0.64 ± 0.03	42.9 ± 0.04	39.6 ± 0.03

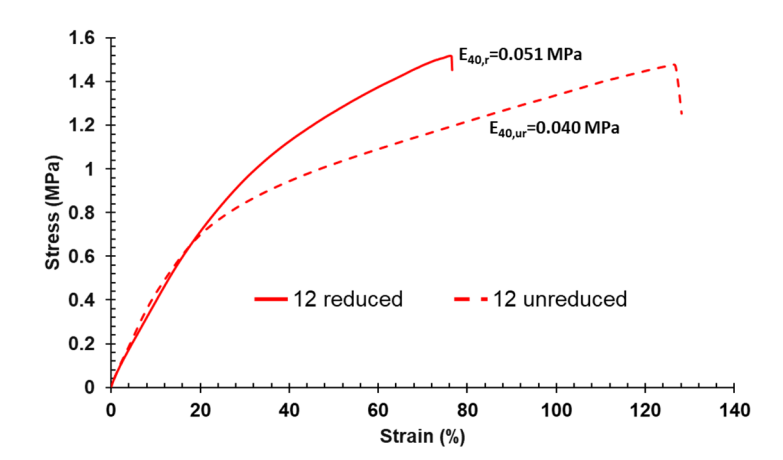


**Figure S18.** Representative stress-strain curves of sample 12 before and after chemical reduction of GO nanosheets.

**Table S4.** Young's modulus of graphene/polymer composites prepared from different methods for comparison to the bijel-templated porous structure reported in this work. S1-S4

Graphene/polymer	Processing	Filler loading (wt%)	Young's modulus (Mpa)	Elongation at break (%)	Ref.
Graphene/PDMS	CVD/polymer coating	0.1	14.4	N/A	[S1]
Graphene/PU	Solution blending	3.0	161	47	[S2]
Graphene/PU	Solution blending	1.0	> 3.0	~ 25	[S3]
Graphene/PDMS	Infiltration into 3D foam	1.2	3.86	39	[S4]
rGO/resin	Interfacial assembly	4.0	0.08	58.7	This work with sample 20

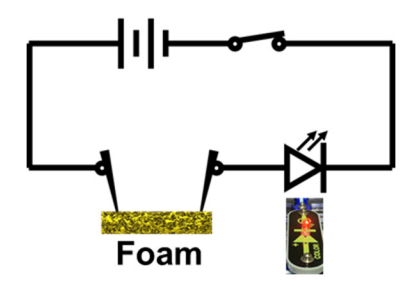


**Figure S19.** Schematic illustration of circuit for light bulb-lighting ability test of sample under peeling test.

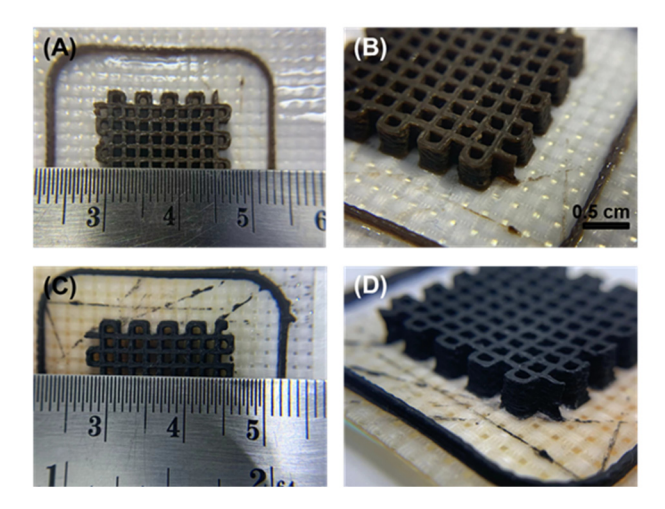


**Figure S20.** Printed cubic lattice of sample 28 before (A and B) and after (C and D) GO nanosheets reduction and water removal.

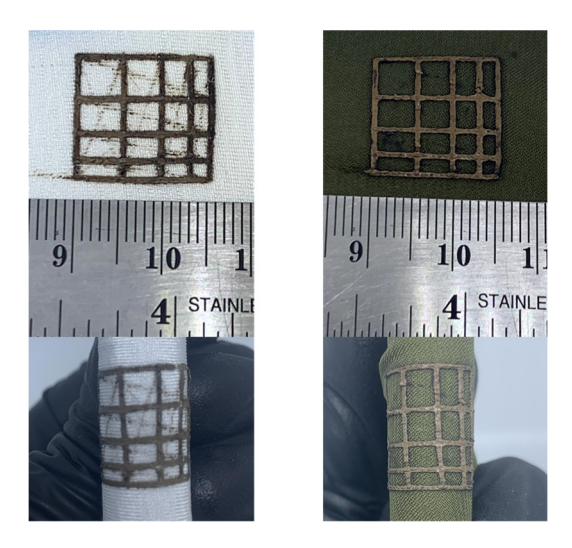


**Figure S21.** Cubic lattice printed onto and deformed 50/50 cotton/polyester fabric (left) and 100% cotton fabric (right).

**Table S5.** RF heating response of particles/polymer composites prepared from different methods in comparison to the bijel-templated porous structure reported in this work. S5-S7

2D nanosheets/polymer	Processing	Filler loading (wt%)	RF frequency /power	Temperature ramp within 2 s under RF	Ref.
Graphene/PVA	Solution mixing	15.0	107 MHz/35 W	< 10 °C	[S5]
MXene/PVA	Solution mixing	5.0	98–100 MHz/1 W	< 5 °C	[S6]
CNT/PLA	Melt compounding	7.5	100 MHz/100 W	< 60 °C	[S7]
rGO/resin	Interfacial assembly	4.0	125 MHz/1 W	215.4 °C	This work with sample 20

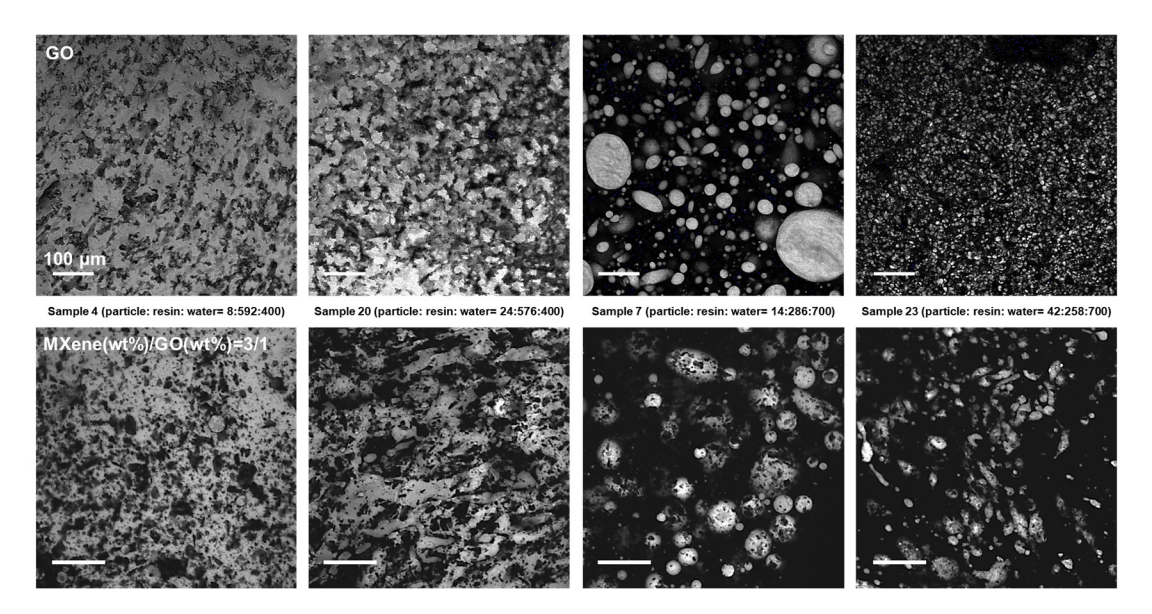


**Figure S22.** Confocal fluorescence microscopy images of inks with same resin, water, and nanosheet ratio but different nanosheet identity. Top: samples prepared with GO nanosheets only. Bottom: samples prepared with 3:1 MXene:GO hybrids. All scale bars are 100  $\mu$ m.

# Reference

- [S1]. Reddy, S.K., Ferry, D.B., and Misra, A. (2014). Highly compressible behavior of polymer mediated three-dimensional network of graphene foam. RSC Advances *4*, 50074-50080. 10.1039/c4ra08321k.
- [S2]. Sofla, R.L.M., Rezaei, M., Babaie, A., and Nasiri, M. (2019). Preparation of electroactive shape memory polyurethane/graphene nanocomposites and investigation of relationship between rheology, morphology and electrical properties. Composites Part B: Engineering *175*, 107090. 10.1016/j.compositesb.2019.107090.
- [S3]. Mei, S., Zhang, X., Ding, B., Wang, J., Yang, P., She, H., Cui, Z., Liu, M., Pang, X., and Fu, P. (2021). 3D Printed thermoplastic polyurethane/graphene composite with porous segregated structure: Toward ultralow percolation threshold and great strain sensitivity. Journal of Applied Polymer Science *138*, 50168. 10.1002/app.50168.

- [S4]. Jun, Y.-S., Park, M.G., Um, J.G., Habibpour, S., Sy, S., Park, C.B., and Yu, A. (2020). The conductivity of polydimethylsiloxane/graphene nano-ribbon foam composite with elongation. Carbon *162*, 328-338. 10.1016/j.carbon.2020.02.024.
- [S5]. Debnath, D., Zhao, X., Anas, M., Kulhanek, D.L., Oh, J.H., and Green, M.J. (2020). Radio frequency heating and reduction of graphene oxide and graphene oxide-polyvinyl alcohol composites. Carbon *169*, 475-481. 10.1016/j.carbon.2020.07.076.
- [S6]. Habib, T., Patil, N., Zhao, X., Prehn, E., Anas, M., Lutkenhaus, J.L., Radovic, M., and Green, M.J. (2019). Heating of Ti3C2Tx MXene/polymer composites in response to Radio Frequency fields. Scientific reports *9*, 16489. 10.1038/s41598-019-52972-2.
- [S7]. Sweeney, C.B., Moran, A.G., Gruener, J.T., Strasser, A.M., Pospisil, M.J., Saed, M.A., and Green, M.J. (2018). Radio frequency heating of carbon nanotube composite materials. ACS applied materials & interfaces *10*, 27252-27259. 10.1021/acsami.8b06268.